The Pennsylvania State University

The Graduate School

Department of Electrical and Computer Engineering

DAYTIME PERFORMANCE OF THE LAMP RAYLEIGH/RAMAN LIDAR SYSTEM

A Thesis in

Electrical Engineering

by

David W. Machuga

Submitted in Partial Fulfillment
of the Requirements
for the Degree of

Master of Science

May 1993

We approve the thesis of David W. Machuga.

Date of Signature

Charles R. Philbrick Professor of Electrical Engineering Thesis Advisor	
Lynn A. Carpenter Associate Professor of Electrical Engineering	
Anthony J. Ferraro Professor of Electrical Engineering	
Raymond J. Luebber Professor of Electrical Engineering	
John D. Mathews Professor of Electrical Engineering	
Larry C. Burton Professor of Electrical and Computer Engineering Head of the Department of Electrical and Computer Engineering	

Abstract

The daytime performance of the LAMP (Laser Atmospheric Measurement Program) has been characterized and will be presented. The construction of the LAMP system was completed at Penn State University during the summer of 1991. It was developed to measure molecular density from the ground to 80 km, and concentrations of nitrogen (N_2) and water vapor (H_2O) from the ground to 35 km and 5 km, respectively. These measurements were to be obtained initially at night and eventually into daylight conditions. An introduction to the LAMP system, as well as scattering, filtering, and LOWTRAN 7 atmospheric modeling fundamentals are presented. Several day-sky background reduction techniques are compared and the potential effectiveness of each method is discussed. The performance of the LAMP system under daylight conditions is shown with different system configurations for comparison. In addition, future upgrades to improve the daytime performance of the LAMP system are outlined. The daytime analysis of the LAMP system emphasizes several daylight performance enhancing techniques such as limiting the field of view of the telescope, use of narrowband filters, high blocking filters, and the exploitation of the solar blind region by using the 4th harmonic from of the Nd:YAG at 266 nm, and the effect on overall system operation to produce an improved instrument.

Table of Contents

List of Figures

Acknowledgments

I have many people whom I am indebted to for help that went seemingly unappreciated. Much of the work in this thesis would not have been possible without the help of the Lidar graduate students. I sincerely thank Tim Stevens, Paul Haris, Subha Maravada, Sumati Rajan, Yi-Chung Rau, George Evanisko, Steve McKinley, Mike O'Brien, Brian Mathason, Jim Anuskiewicz, and Jim Yurack for their help with my work. In addition, I would like to recognize Dan Lysak, Tim Kane, Tom Petach, Glenn Pancoast, and Karen Brooks for their contributions as well.

Many others were of great help with this thesis. The Department of Electrical Engineering has many people to whom I will always be grateful. Some of these include, Glenna, Lisa, Linda B., Linda K., Janet, and Connie, as well as many more. Thanks again!

I am also grateful for the help and guidance provided by my committee. The insight of C. R. Philbrick, Lynn A. Carpenter, Anthony J. Ferraro, Raymond J. Luebbers, and John D. Mathews is appreciated, and I will learn from my experiences with all of them.

There are two of my friends that deserve special mention in my thesis, Ray Hughes and Mike House. Ray, thanks for all of your help through both undergrad and grad. I don't know if I ever said thanks, but thanks. Mike, I was best man at your wedding, and that was very important to me. I am glad I have the privilege of being your friend. Thanks for everything.

As any thesis author has experienced, the last week of writing is the worst. I owe a great deal to two people who helped me through all of it, Subha and Sumati. Subha, I am graduating at the same time with you and we spent a week in the lab writing our thesis. I am glad you were here. Sumati, I am in your debt for teaching me many things, and I wish to thank you for your support while I was writing my thesis. Thanks for caring.

Finally, I wish to thank my parents who have supported me, both emotionally and financially all of my life. I could never have done this with out you, I love you both.

Chapter 1

Introduction

The atmosphere is becoming a focus of attention and concern due to a number of developing problems. Many of the concerns focus on several particular issues, such as, the depletion of ozone resulting in harmful levels of ultraviolet radiation reaching the earth's surface, the increase of carbon dioxide and other greenhouse gases in the warming of the environment, the role that aerosols play in causing substantial changes in the global climate, and smog formation in many major cities becoming a health hazard.

Several methods have been developed to monitor atmospheric properties, including meteorological rockets, weather balloons, cloud radars, and lidar. The most promising method for widespread use to measure the current state and monitor the changes in the atmosphere is lidar. Lidar (LIght Detection And Ranging) operates similarly to radar except light is used instead of radio waves.

The first lidar employed a searchlight and telescope in a bistatic configuration to measure atmospheric density[1]. Lidar measurements became a viable method for atmospheric remote sensing with the advent of the laser, and particularly the pulsed laser[2], which allowed the development of high range resolution instruments and data returns from higher altitudes.

Currently, lidar systems are widely used as a research tool to measure atmospheric properties[3]. Measurements of these properties are needed in routine data collection programs for a complete environmental monitoring system. Measurement techniques

ranging from simple Rayleigh scattering profiling to resonant fluorescence measurements of mesospheric iron and sodium, as well as vibrational Raman profiles to determine water vapor and nitrogen content, aerosols, and several other constituents, can be utilized to monitor the atmosphere. Lidar systems have been used for atmospheric chemical analysis, and the monitoring of atmospheric layering processes and will someday be used in weather forecasting. Even the dust layers resulting from the 1991 eruption of Mt. Pinatubo have been profiled and are currently being monitored and compared to other measurements[4,5,6].

Lidar systems provide very high spatial and temporal resolution measurements. However, most of the measurements previously listed cannot be obtained during daylight hours. This is an extreme limitation since many of the chemical reactions and thermal layering processes are a result of direct solar radiation.

We have developed a new method to obtain reliable density measurements to 50 km, and Raman measurements to over 5 km under conditions of direct sunlight. This technique employs an adjustable iris as a field stop, a thermally stabilized narrowband filter, and a continuously optimized Fabry-Perot etalon to isolate the laser backscatter from the broadband background illumination. This thesis will present calculations of system performance and measured values from the system. Additionally, a new electrical and optical system design for tuning a Fabry-Perot etalon to a laser wavelength will be introduced. However, before the daytime system design is discussed, some theory in atmospheric remote sensing and optical system elements will be reviewed.

1.1. Lidar Principles of Operation

Lidar operates similarly to radar techniques applied to optical wavelengths. The transmitter is usually a pulsed laser. Laser pulses are normally directed to the zenith and the backscattered return is monitored. The backscatter can result from four scattering processes, these are: 1) Rayleigh scattering, 2) aerosol or particulate scattering, 3) Raman (vibrational and rotational) scattering, and 4) resonance scattering (which is not relevant to the current Penn State system). For completeness, the three relevant processes are briefly outlined here.

1.1.1. Molecular Scattering

Molecular scattering is also commonly called Rayleigh scattering, however the term molecular scattering is chosen here since it applies not only to the central unshifted Cabannes line, but to the Stokes and anti-Stokes lines on either side of the Cabannes line[7]. This type of scattering occurs when the scattering particle is much smaller then the wavelength of the incident light. Therefore, molecular scattering is the predominate scattering mechanism at higher altitudes, above 30 km, where there exist negligible aerosol or particle scattering contributions.

The backscattering cross section for molecular scattering is defined by,

$$\sigma_{\pi}{}^{M}(\lambda) = \frac{\pi^2 (n-1)^2}{N^2 \lambda^4} \quad ,$$

where n is the index of refraction, N is the number of scatterers, and λ is the wavelength of the incident light. This shows the well known λ^{-4} dependence of cross section associated with the molecular backscattering process which results in a five times greater

molecular backscatter cross section at 355 nm than at 532 nm.

It should be noted that the molecular backscatter will have a Doppler broadened backscatter spectrum which is dependent on temperature. Although this broadening of approximately 1.2 GHz is not critical to normal operation of most lidars, it will become important for the newly developed wind sensor, which is described in Chapter 6.

1.1.2. Aerosol (Particulate) Scattering

Aerosol scattering is commonly referred to as Mie scattering, however the Mie scattering theory only applies to spherical particles, and it also encompasses the small particle limit of Rayleigh scattering. Aerosol scattering is an elastic scattering process that occurs when the size of the scattering particle is on the order of, or larger than, the wavelength of the incident light. Since these particles are large, their velocities are low and the effect of thermal Doppler broadening is negligible.

The calculation of the backscattering cross section for aerosol scattering is a function of size for spherical particles, and for non-spherical particles is a complex function of the size and shape. For a review of this area, several references exist[8], but a complete discussion is beyond the scope of this thesis.

1.1.3. Raman Scattering

There are two types of inelastic scattering, Raman vibrational and rotational. The inelastic scattering processes which involve the vibrational states result in a shift on the order of 100's to 1000's cm^{-1} and those involving the rotational states result in a shift of 10's to 100's cm^{-1}. Both processes are, of course, species dependent. Since Raman scattering is unique to the species, it allows relative concentration measurements of

constituents independent of aerosol scattering in the lower atmosphere when the laser energy extinction profile can be quantified.

Raman scattering can be explained by starting with a molecule in an arbitrary vibrational ground state N_o (Q-branch). This molecule is then illuminated by laser light and elevated to an excited virtual state, M. The molecule may spontaneously decay to another vibrational state, N_1, that is characterized by a higher energy than N_o. The scattered wavelength has energy $M - N_1$ ($< M - N_o$), which results in the characteristic Stokes lines particular to the vibrational energy states of this molecule. If the transition was to state N_{-1} which is lower in energy than N_o, the scattered wavelength would have energy, $M - N_{-1}$, which is higher energy than the incident light and the transition is referred to as the anti-Stokes line.

Rotational Raman scattering is similar to the vibrational process except that the energy difference for rotational states is smaller than vibrational and the population distribution of the rotational states depends on temperature. Vibrational Raman lines Q-branch also have rotational Raman lines which surround their central peak.

There are several Raman scattering wavelengths that are currently used by the Penn State LAMP lidar system. The vibrational Raman scattering wavelengths from the 532 nm laser output are 607 nm and 660 nm, characterizing nitrogen (N_2) and water vapor (H_2O), respectively. In addition, a monitoring technique used to measure temperature using the rotational Raman anti-Stokes lines at 530 nm and 528 nm has been implemented.

Once the laser energy is scattered by the atmosphere, the backscattered energy

must be analyzed. The returning light is collected by a telescope, filtered by an optical system, measured by a detector, and quantified by a data system. This receiver may be as simple as a photomultiplier tube (PMT) attached behind a telescope with one filter, or may consist of several detectors with a complex optical path including beamsplitters, filters, and other elements to separate the different wavelengths.

1.2. Lidar Equation

With all of the different scattering processes, optical elements, lasers, atmospheric conditions, etc..., prediction of the performance of a lidar system becomes important. This is true not only for modeling a new system, but also when analyzing the returns of the current system. To quantify most factors affecting the return signal, the lidar equation is introduced as,

$$N(z) = \frac{E_L}{hc/\lambda_L} * T(\lambda_L,z)\,T(\lambda_S,z) * \sigma(\lambda_L,\lambda_S)\,n(z)\,\Delta z * \frac{\xi(z)A_0}{4\pi z^2} * \xi_{eff}(\lambda_S) \quad .$$

(1) (2) (3) (4) (5) (6)

The terms of this equation are split for descriptive purposes. The grouped terms are: (1) the predicted photon count from range z, (2) the number of transmitted photons from the laser, (3) the one way atmospheric transmission from the ground to the scattering altitude z at the laser wavelength and the scattered wavelength, (4) the probability of scattering in the illuminated volume or range bin, (5) the probability of collecting the scattered photons from altitude z, and (6) the optical efficiency of the detector system. Each of the terms in the lidar equation will be explained further in the following sections of this thesis as well as the application of this equation to the Penn State LAMP lidar system. A

description of the Penn State LAMP lidar is given in the next section to familiarize the reader with this system.

1.3. Penn State's LAMP Lidar

Design work on the Penn State LAMP (Laser Atmospheric Measurements Program) lidar system was started in October of 1989. The design was centered around the concept of a self-contained transportable instrument which could be operated in the field in most weather conditions. The assembly of the system was begun during Fall 1990 and the system began operational testing in June 1991. The instrument was transferred from the Electrical Engineering East building to a modified shipping container that has been used as a field laboratory since July 1991.

After a testing period at Penn State, the lidar container was shipped to Andenes, Norway for participation in the LADIMAS (LAtitudinal DIstribution of Middle Atmospheric Structure) measurement campaign. This campaign included measurements on board the RV Polarstern as the ship sailed from Tromso, Norway, to Bremerhaven, Germany, then to Argentina, Antarctica, and finally to Chile.

The lidar system is composed of five basic subsystems. These subsystems are the transmitter, receiver, detector, data acquisition/recording, and control/safety. The transmitter, receiver, and detector of the LAMP system are shown in Figure 1.1. The data acquisition/recording and control/safety subsystems are located in an instrument rack.

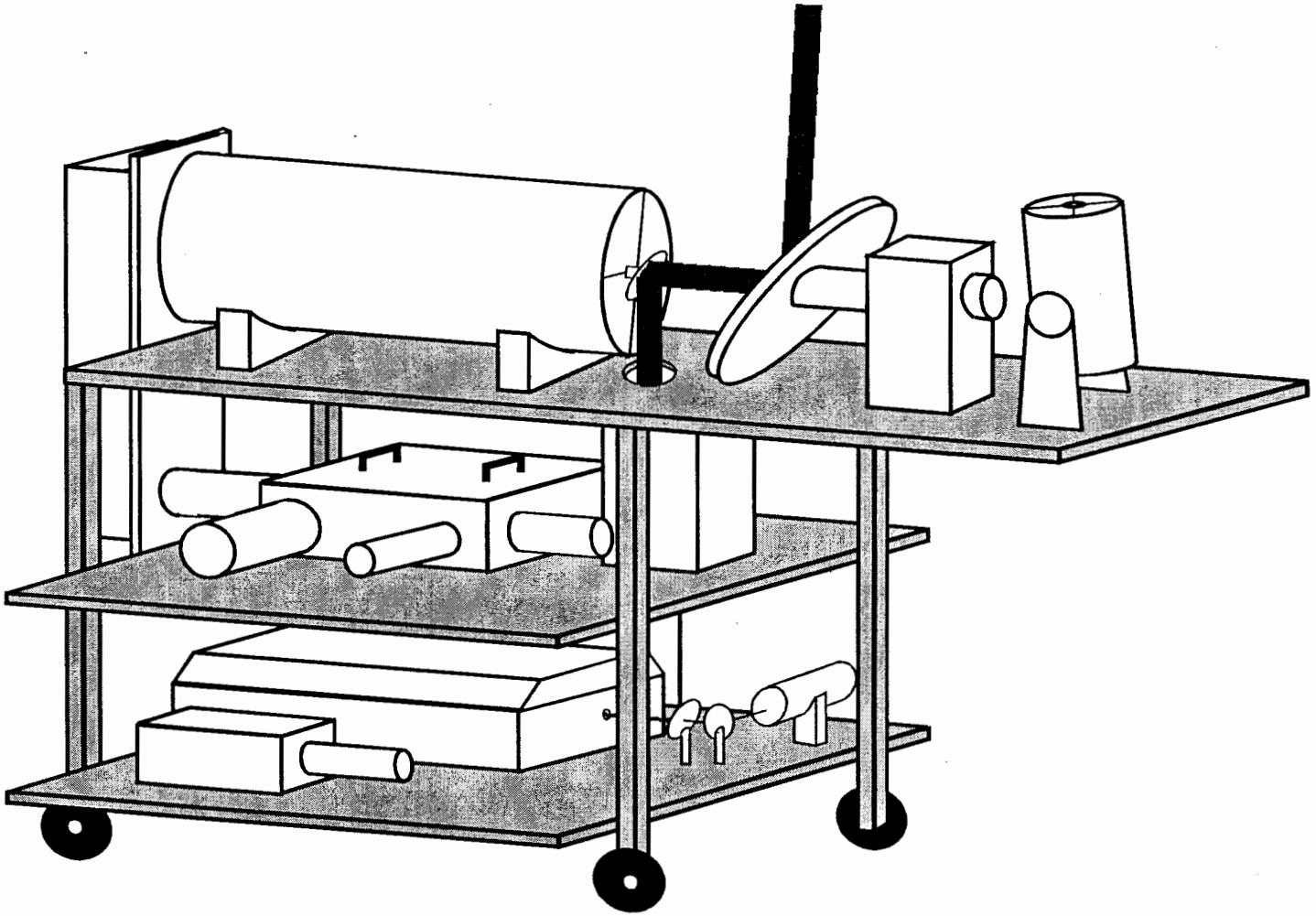

Figure 1.1 -- Drawing of the LAMP instrument and three of its five subsystems: transmitter, receiver and detector[9].

1.3.1. Transmitter

The transmitter of the LAMP system is a Nd:YAG laser, Continuum Model NY82, and is located on the bottom shelf as shown in Figure 1.1. This laser outputs 1.5 J per pulse at a fundamental wavelength of 1064 nm at a pulse rate of 20 Hz. The laser's fundamental wavelength is doubled (to 532 nm) and tripled (to 355 nm) by nonlinear crystals to produce the combined output. The final output energy is 600 mJ at 532 nm and 250 mJ at 355 nm; the 1064 nm output is approximately 150 mJ but is not used by this system. The laser energy is directed at the zenith via a beam expander and three laser hard coated mirrors.

1.3.2. Receiver

The scattered energy is collected by the receiver which is a f/15 Cassegrain telescope. The telescope has a focal length of 6.09 m, a primary diameter of 40.6 cm, and a secondary diameter of 10.2 cm. This telescope is horizontally mounted and has a 61 cm optical flat to direct the field of view (f.o.v.) vertically. The original design incorporated beam forming optics after the telescope to collimate the light before the detector, but this has been replaced by a fiber optic link with a NA of 0.22, which corresponds to a full angle of approximately 50 degrees and diameter of 1 mm. Both the optical flat and the telescope are shown in Figure 1.1 on the top shelf of the table.

1.3.3. Detector

The detector subsystem[9] is shown in Figure 1.1 on the middle shelf. The detector is equipped with six separate channels which include the 532 nm high and low altitude, 355 nm high and low altitude, and two vibrational Raman channels, one for nitrogen (607

nm), and one for water vapor (660 nm). The 532 nm and 355 nm low altitude PMT's are uncooled and simply digitize the analog return signal. All other channels have cooled housings to reduce dark current and operate in photon counting mode. An internal layout of the detector is shown in Figure 1.2 which includes the PMT's and other processing optics listed after the figure.

The return signal enters from the top of the detector box as shown. After the initial pass through the shutter wheel (29), the signal is split by a beamsplitter (2) which reflects the 532 nm return and transmits the 355 nm, 607 nm and 660 nm returns. Following the 532 nm path, the light passes through the Fabry-Perot etalon (3) and thermally stabilized filter (4) for narrow band filtering. Another beamsplitter (5) transmits 0.64% of the return to the 532 nm low altitude digitizing PMT. The reflected signal is shuttered (29) again to prevent the low altitude signal from saturating the photon counting PMT's. The remaining signal is then detected by the high altitude photon counting PMT.

The 355 nm return path is similar with the exception of an additional beamsplitter (15) and the filter (23) is not as narrow as in the 532 nm path. The beamsplitter reflects the Raman 607 nm and 660 nm returns and transmits the 355 nm return. The Raman returns are again split by another beamsplitter (16) which reflects 660 nm and transmits 607 nm. Both Raman channels have narrowband filters (17, 20) for background noise and laser line rejection. These filters have a 0.3 nm bandpass, similar to the filter used in the 532 nm path.

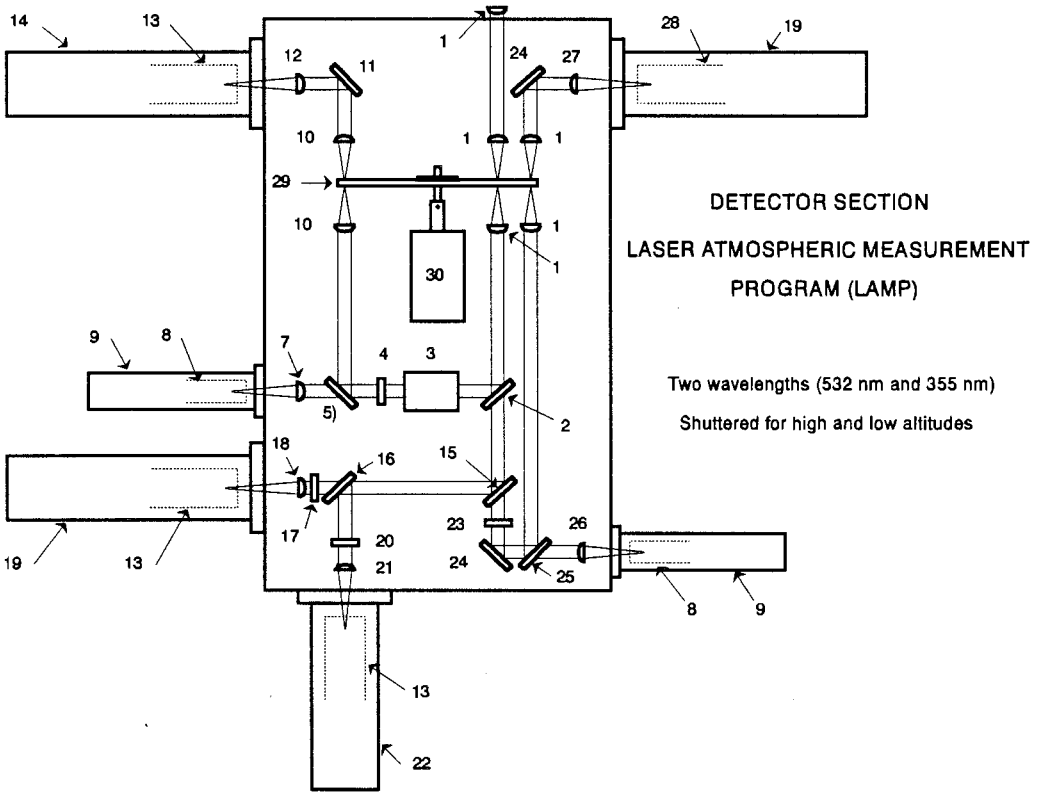

Figure 1.2 -- Schematic Drawing of the Detector Section for the LAMP Lidar [9]

Key to Figure 1.2

1a-d) Fused silica plano-convex lens, d = 25.4 mm, F = 50.8 mm, AR coated for 355, 532, 607,and 660 nm.

2) Dichroic beam-spitter, d = 50.8 mm, splits off 532 nm from 355, 607 and 660 nm.

3) Fabry-Perot etalon, electronically tuned to transmit 532 nm with a 0.01 nm bandwidth.

4) 532 nm narrow band-pass filter with a 0.29 nm bandwidth, temperature stabilized at 34° C.

5) 532 nm beam-spitter.

7) Glass plano-convex lens, d = 25.4 mm, F = 175 mm, AR coated for 532 nm.

8) 28 mm Thorn EMI 9828B03 PMT, analog data which is digitized, (2 ea.).

9) 28 mm Thorn EMI socket and housing assembly.

10a-b) Glass plano-convex lens, d = 25.4 mm, F = 50.8 mm, AR coated for 532 nm.

11) 532 nm high reflectivity mirror, d = 50.8 mm.

12) Glass plano-convex lens, d = 25.4 mm, F = 200 mm, AR coated for 532 nm.

13) 52 mm Thorn EMI 9863B/350 PMT, photon counting, (2 ea.).

14) 52 mm Thorn EMI thermoelectric cooled (-25° C) PMT socket and housing .

15) Dichroic beam-spitter, d = 50.8 mm, splits off 355 nm from 607 and 660 nm.

16) Dichroic beam-spitter, d = 50.8 mm, splits off 607 nm from 660 nm.

17) 607 nm band-pass filter, with a 0.3 nm bandwidth.

18) Glass plano-convex lens, d = 25.4 mm, F = 62.9 mm, AR coated for 607 nm.

19) Amherst Scientific thermoelectric cooled (-30° C) PMT socket and housing .

20) 660 nm bandpass filter, with a 0.3 nm bandwidth.

21) Glass plano-convex lens, d = 25.4 mm, F = 200 mm, AR coated for 660 nm.

22) Pacific Research thermoelectric cooled (-25° C) PMT socket and housing.

23) 355 nm bandpass filter, with a 3.2 nm bandwidth.

24a-b) 355 nm high reflectivity mirror, d =50.8 mm.

25) 355 nm beamsplitter.

26) Fused silica plano-convex lens, d = 25.4 mm, F = 175 mm, AR coated for 355 nm.

27) Fused silica plano-convex lens, d = 25.4 mm, F = 100 mm, AR coated for 355 nm.

28) 52 mm Thorn EMI 9893B/350 PMT, photon counting.

29) Aluminum high speed (4800 rpm) optical chopper wheel, d = 10 inches.

30) Hysteresis synchronous motor for the chopper wheel.

31) General purpose optical mirror, d = 50.8 mm.

32) General purpose optical mirror, d = 50.8 mm.

33) Glass plano-convex lens, d = 50.8 mm.

34) Glass plano-convex lens, d = 50.8 mm.

1.3.4. Data Acquisition/Recording

The PMT's produce signals proportional to the incident light intensity. These signals are converted from current pulses to either voltages for digitizing or NIM level signals for photon counting. The converted signals are then recorded by a set of CAMAC data acquisition modules. Once per minute the data in the CAMAC crate is transferred to a 486 PC for storage on a 1 GB WORM optical disk. The PC also creates a 30 minute accumulated file that is also stored on optical disk.

1.3.5. Control/Safety

The control system circuitry was designed and built in-house. The laser flashlamps, Q-switching, and data acquisition timing are controlled by this circuit. For a complete discussion of the system and circuits, the reader is referred to Stevens thesis[9].

The safety system consists of laser interlocks, control panel panic buttons, and a radar aircraft avoidance system. These systems are also not within the scope of this thesis but a complete discussion may be found in the safety plan for the LAMP lidar[10].

1.4. Outline of Thesis

This thesis will outline the daytime measurement capabilities of the LAMP lidar system. The day-sky background, as modeled by the Lowtran 7 model, will be discussed in Chapter 2. Chapter 3 includes discussion of filtering techniques that use narrowband multilayer interference filters and a Fabry-Perot etalon. Chapter 4 covers several background reduction techniques and their potential effectiveness. Comparisons have been made between predicted performance based on models and results from measured performance of the LAMP system in Chapter 5. In Chapter 6, future work in this area

as well as wind measurements which draw on several concepts developed in the thesis will be discussed.

Chapter 2

Day-Sky Values

Lidar measurements provide high resolution spatial and temporal measurements. However, these measurements are difficult to obtain when there is a significant background noise present, such as in the case of daytime measurements. To better understand the measurement difficulties, this chapter will discuss a model of solar background based on Lowtran 7. Measurements of the solar background have been made to verify the model results, and these results are related to the LAMP lidar instrument.

2.1. Model of Solar Background (Lowtran 7)

The Air Force Geophysics Laboratory (AFGL), originally called the Air Force Cambridge Research Laboratories, developed an atmospheric model of electro-magnetic effects for the wavelength range of 0.25 - 28 μm in the early 1970's[11]. Initially, the results were compiled and displayed in a set of charts and graphs. The computer models contained in Lowtran were created to consolidate several atmospheric and geophysical calculations[12]. It includes calculations for atmospheric transmittance, background radiance, single scatter solar and lunar radiance, direct solar irradiance, and multiple scattered solar and thermal radiance.

The Lowtran 7 model[13] now contains six model atmospheres which are stratified into 1 km layers up to 25 km, and larger layers up to 100 km. The model also contains 10 different boundary-layer aerosol models, 8 different stratospheric extinction models (volcanic), as well as, seasonal variations, precipitation and cloud models.

As an example of Lowtran 7 calculations, Figure 2.1 shows the atmospheric transmission from zero to 1, 2, 3, 4, and 5 km. The transmission variations are due to absorption by atmospheric species, molecular scattering, and small amounts of particulate scattering. Values from this plot will be used in Chapter 4 to calculate predicted lidar returns.

2.2. Quantification of the Day-Sky Background

Assuming the Lowtran calculations are correct, the resulting data must be quantified in units relevant to the LAMP system. Lowtran provides solar irradiance and radiance values which must be applied to the system. To set up the analysis of the system, it is necessary that two parameters be introduced, irradiance and radiance[14].

2.2.1. Irradiance

Irradiance is defined as the integrated radiant flux per unit area. To introduce the idea of irradiance, let us assume that the output of a solar cell is to be calculated. The detector has an active area *da'* in square meters and is placed perpendicular to the light from the sun as shown in Figure 2.2. The output would be proportional to the irradiance incident on the detector, assuming all incident energy, regardless of wavelength, is absorbed. This effect is an integration of all light over the hemisphere above the detector without regard to direction.

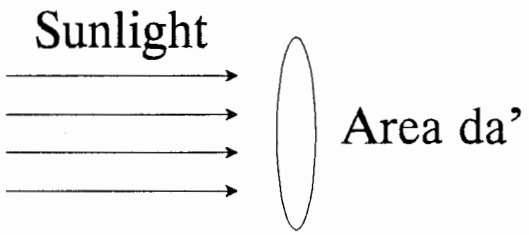

Figure 2.2 -- Solar Irradiance Detector

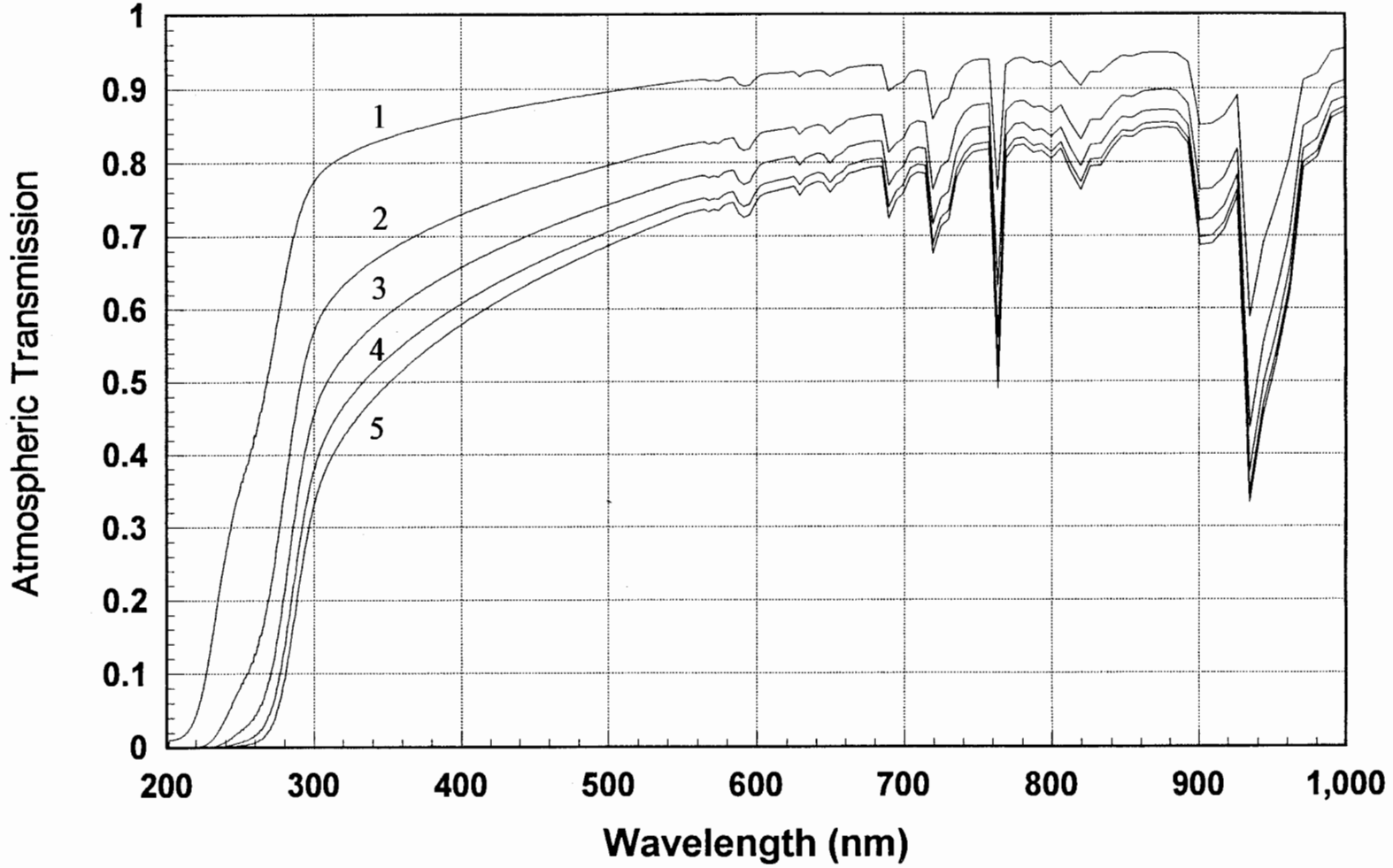

Figure 2.1 -- Atmospheric Transmission from the Surface to 1, 2, 3, 4, and 5 km from Lowtran 7 Assuming 5 km Visibility

The Lowtran calculation of solar irradiance before and after atmospheric transmission effects is shown in Figure 2.3. The lower curve is the solar irradiance on the Earth's surface due to the incident solar irradiance on the atmosphere represented by the upper curve. The fine structure features in the upper curve are the Fraunhoffer absorption lines due to the highly ionized plasma in the solar corona. The added fine structure and band features of the lower curve are due to absorption by atmospheric species, particularly H_2O, CO_2 and O_2 as well as molecular scattering.

If the detector has an optical bandwidth, this will reduce the measured irradiance. To account for this reduction, irradiance is generally stated with units of Watt m^{-2} μm^{-1}. The micron, μm, in the denominator is the system optical bandwidth of the detector. For example, if the detector had a bandwidth of 0.1 micron, the result would be an integration over all wavelengths within 50 nm of the center wavelength value.

The LAMP optical receiver system has a narrow field of view. As a result, irradiance is not appropriate to calculate the background solar flux into the system. To accurately predict the background, a spatially limited parameter unit should be used. This unit of measure is called radiance.

2.2.2. Radiance

Radiance is defined as the radiant flux per unit area per steradian. Using the detector mentioned in Section 2.2.1. again, the detector is placed such that the diameter of the emitting surface is small compared to the distance to the detector and initially the emitter is assumed to be a flat surface and the only source present. We can then draw a cone from each elemental area *da* on the emitter with the base being the size of the

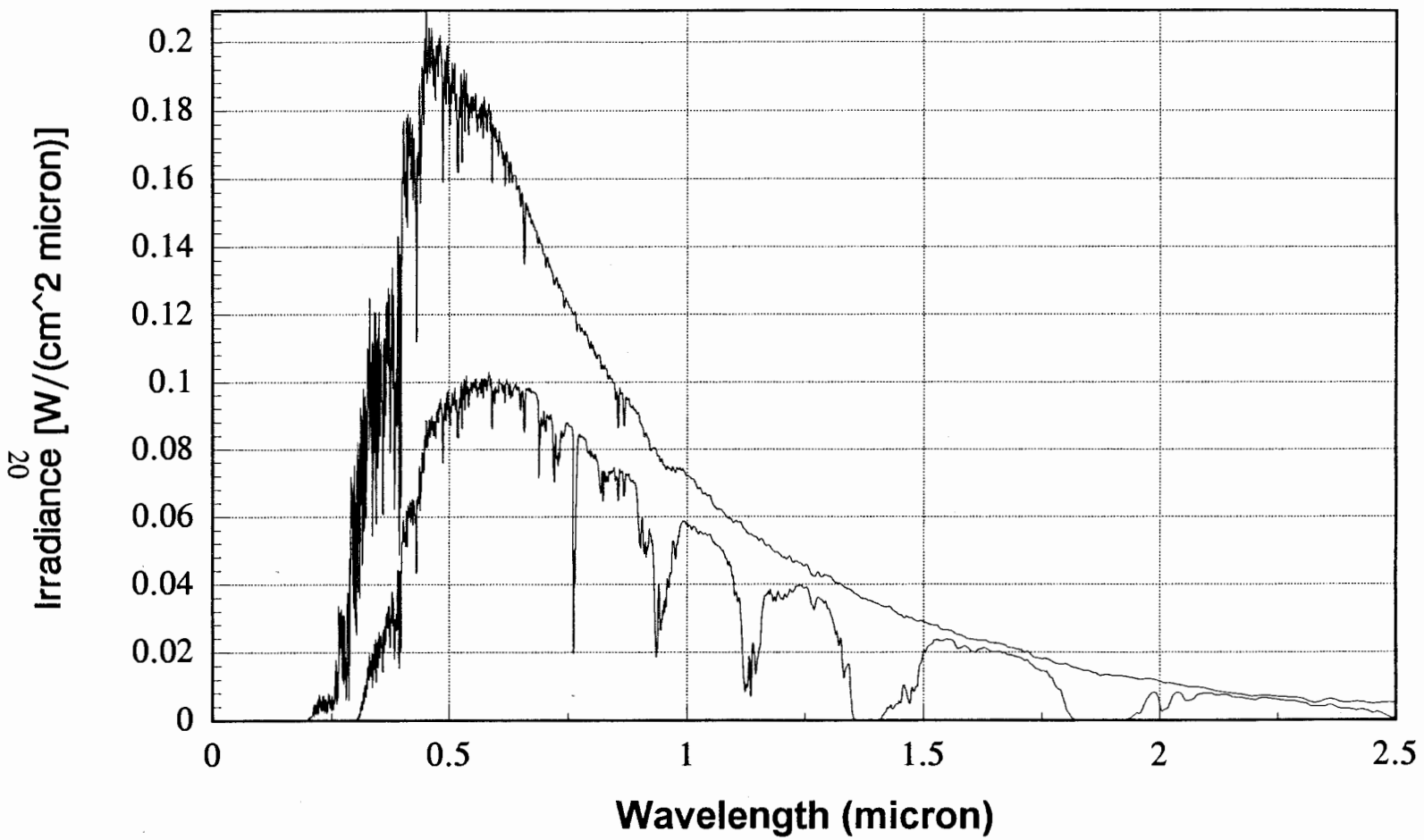

Figure 2.3 -- Solar Irradiance Above the Earth's Atmosphere (upper curve) and at Sea Level (lower curve) from Lowtran 7 Assuming 5 km Visibility

detector as shown in Figure 2.4.

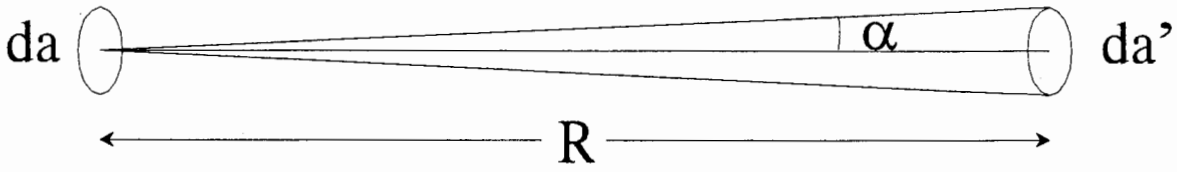

Figure 2.4 -- Geometry of Radiance Definition

The radiant flux arriving at the receiver is proportional to the solid angle, $d\Omega(\alpha)$, and the area *da* of the emitter. This results in the received power equal to,

$$P = L \cdot da \cdot d\Omega(\alpha) = L \cdot da \cdot \frac{da'}{R^2} \ [W] \quad ,$$

where R is the distance between the source and the emitter and L is defined as the radiance and is represented by,

$$L = \frac{radiant\ flux}{(area)\cdot(solid\ angle)} \left[\frac{W}{m^2\ sr} \right] \quad .$$

For the example of solar radiance as viewed from the earth, the solid angle created by the photosphere is approximately 6×10^{-5} sr corresponding to the half degree of the disk viewed from the earth. The resulting calculated radiance is 2.25×10^7 W/(m^2 sr) which represents the detector f.o.v. being sufficiently small as to only encompass the photosphere.

This calculation assumes that there is no scattering processes in the medium in which the detector is located and the detector f.o.v. is such that only the emitter is

viewed. Normally this is not the case and scattering, both single and multiple, must be taken into account. This is generally not an easy calculation for solar radiance since atmospheric conditions are extremely variable, especially in the boundary layer where multiple scattering can dominate. A simple observation of the solar spectral radiance was done and the resulting data is plotted in Figure 2.5 (after Eiden, 1968)[15]. In this figure, the clear sky radiance is plotted on a log scale against the angle from the center of the solar disk, also on a log scale. This plot represents wavelength integrated radiance over a band of cm^{-1} (wavelength band) and only for a clear sky.

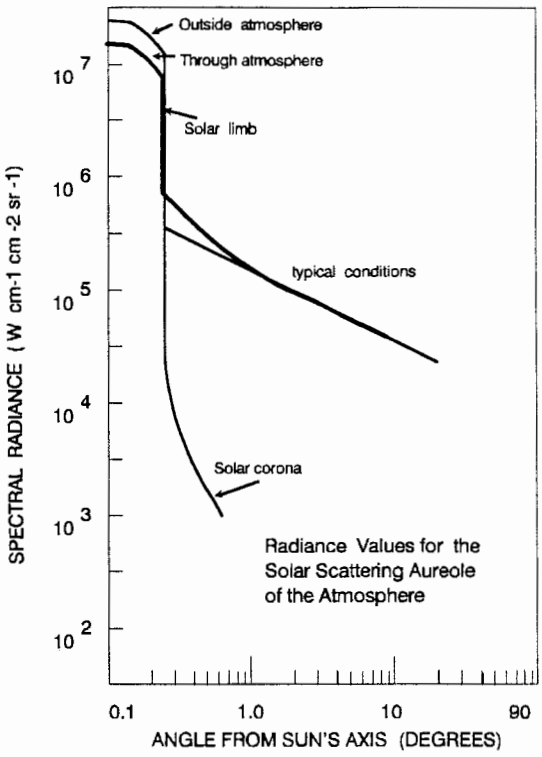

Figure 2.5 -- Solar Spectral Radiance (After Eiden [15])

Lowtran will calculate radiance values with only single scattering and single and multiple scattering based on atmospheric models for different wavelengths. An example calculation with both scattering models was run in Lowtran 7 and the resulting data is plotted in Figure 2.6. It is apparent from the plot that the addition of multiple scattering to the calculation causes the background radiance to increase greatly. This should give a representation of the variability of the day-sky background.

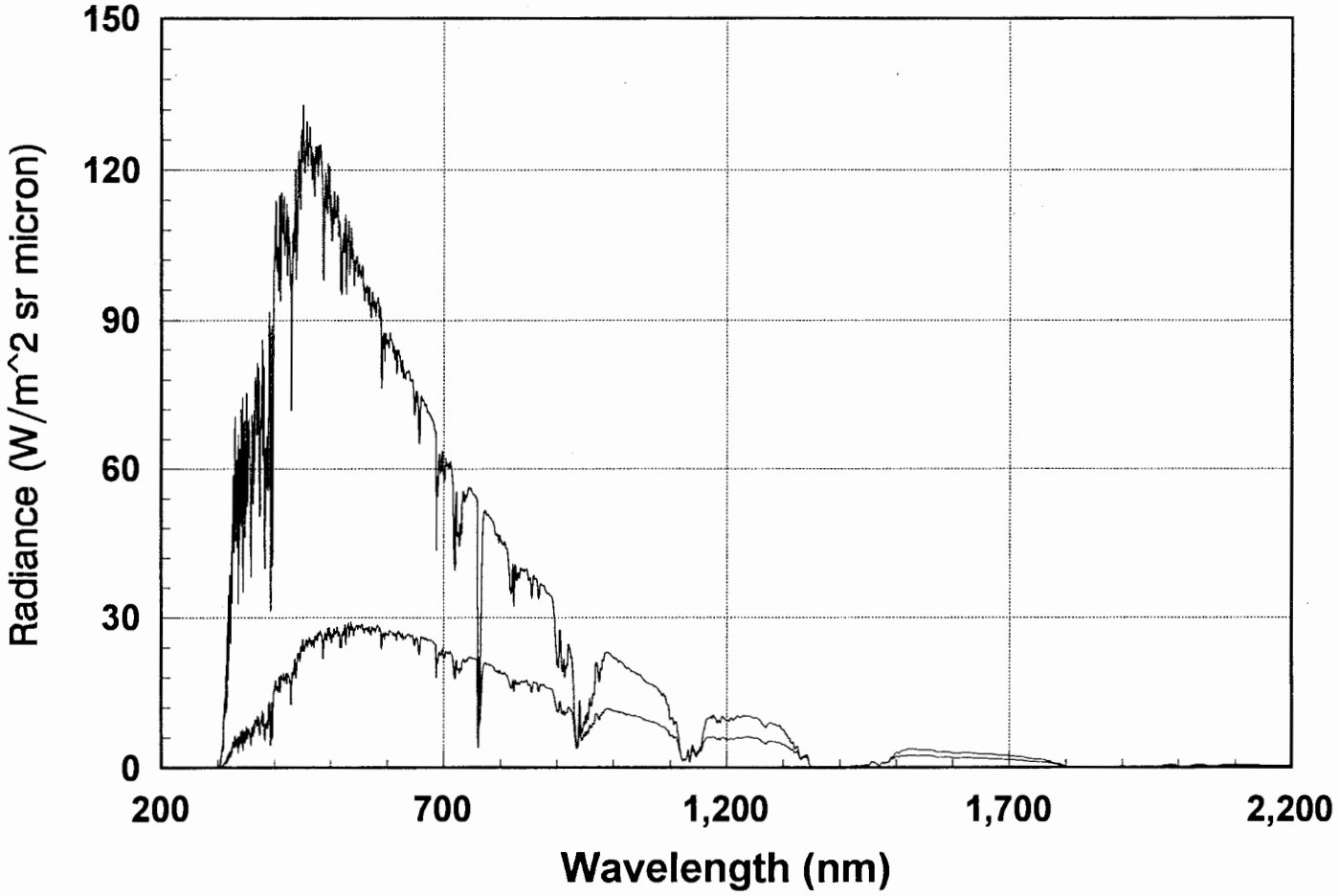

Figure 2.6-- Lowtran Modeled Radiance for Single Scattering (lower curve) and Multiple Scattering (upper curve) Assuming 5 km Visibliity and 60 Degree Solar Zenith Angle

2.2.3. Conversion from Irradiance to Radiance

Dimensional analysis shows a simple conversion from irradiance to radiance, however this is not the case in the atmosphere. With the large variability in the lower atmosphere, simple conversions are not possible. Measurements were made to find a conversion from horizontal diffuse irradiance to radiance under clear sky conditions[16]. These conversion factors may be used to give an approximation to the radiance given the horizontal diffuse irradiance. Results from this paper are shown in Figure 2.7 with a solar zenith angle of 35 degrees. These values are ratios of the irradiance to radiance given various solar azimuth and zenith angles.

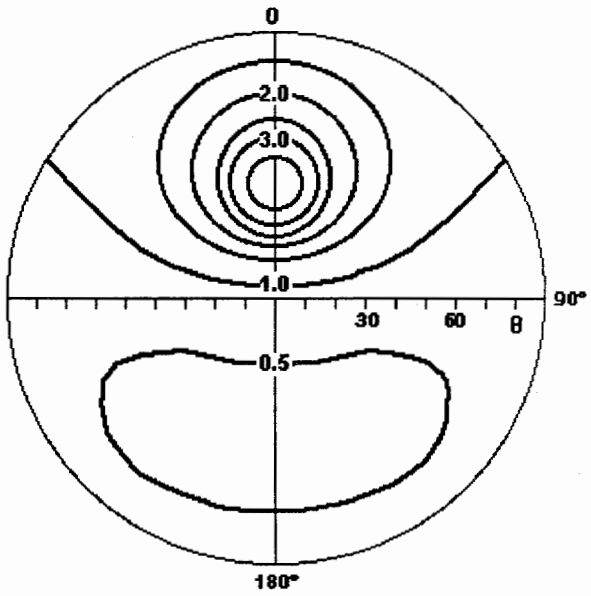

Figure 2.7 -- Ratio of Radiance to Horizontal Diffuse Irradiance (After Steven [16])

2.3 Application to the LAMP Lidar

After measuring the day-sky radiance, the expected background counts can be calculated. The telescope divergence is defined by the field stop which is an aperture that limits the f.o.v.. Measuring the solar radiance received as detected by the LAMP system was done by placing a photodiode placed behind the telescope. Taking measurements at three different solar zenith angles and plotting the data results in Figure 2.8. The

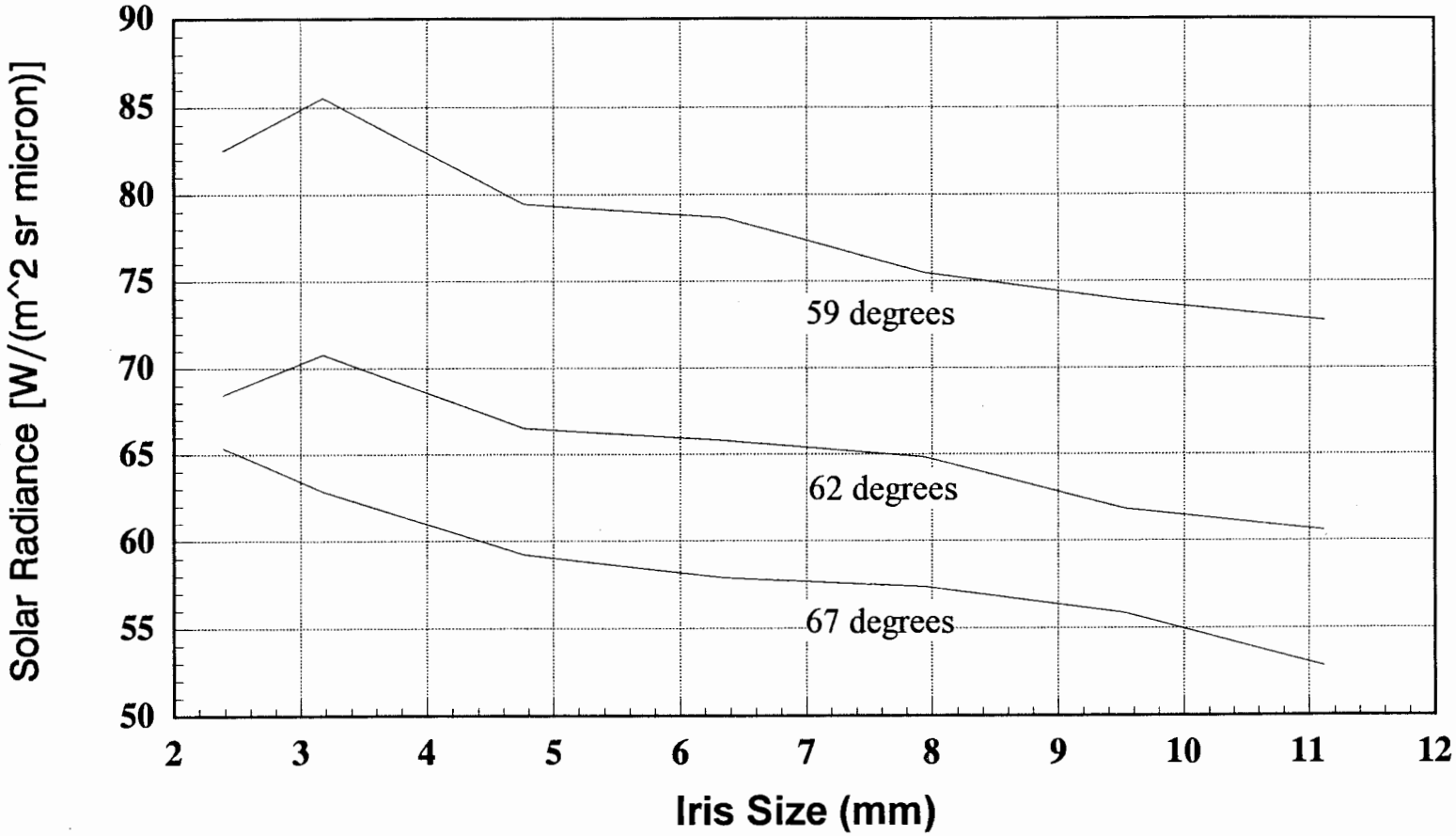

Figure 2.8 -- Radiance Measurements at Three Solar Zenith Angles on November 13, 1992

variation in detected radiance using different iris settings can be explained, since the larger aperture will allow more off-axis rays which are lost in vignetting due to the finite apertures of the optical elements in the system. Reducing the aperture effectively reduces the f.o.v. of the telescope. Application of the field stop to reduce background counts is described in Chapter 4.

The ideal situation that would exist in lidar systems would be to match the telescope field to the laser beam divergence. This would minimize the day-sky background by reducing the surface area from which emitted photons are collected, increasing the signal-to-noise ratio. In general, mechanical vibrations in the instrument limit the extent of this improvement since they may cause the laser to leave the f.o.v. of the telescope causing signal to be lost. Methods for the reduction of the day-sky background will also be discussed in detail in Chapter 4.

Chapter 3

Fabry-Perot Interferometers and Interference Filters

The LAMP system detector box has over 40 optical elements including lenses, beamsplitters, mirrors, and filters. This chapter will concentrate on the filtering optics, i.e. Fabry-Perot interferometers and interference filters, which are important to daytime measurements. For a complete discussion of the other optical elements see Haris' thesis[17].

3.1. Fabry-Perot Interferometers

A Fabry-Perot interferometer is constructed by placing two semi-transparent mirrors parallel to each other separated by a fixed difference, this configuration is usually referred to as an etalon[18]. A monochromatic light incident on an etalon will undergo multiple reflections inside the cavity. The resulting transmission will be a set of bright concentric rings or fringes whose angular displacement is proportional to the spacing of the mirrors and inversely proportional to the wavelength[19].

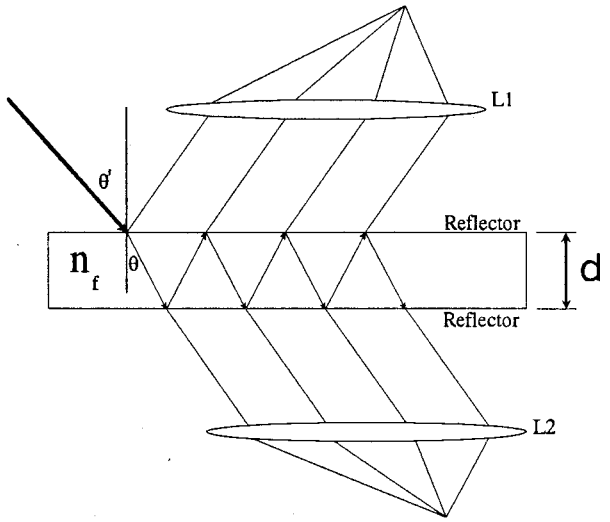

Figure 3.1 -- Multiple Reflections in an Etalon

Let us assume that a plane wave is incident at angle θ' on an etalon having cavity spacing d, and a medium refractive index n_f, as shown

in Figure 3.1. The approach that will be used is to sum the transmission (and reflection) of the infinite number of partial waves produced by the reflections off the two reflectors[20]. The phase delay produced by one trip down and back through the cavity is given by, where λ is the vacuum wavelength of the incident light and θ is the internal angle of incidence. If the complex amplitude of the incident wave is given by A_i, then the partial reflections, B_1, B_2, B_3, . . . , are given by,

$$\delta = \frac{4\pi n_f d \cos\theta}{\lambda} \quad ,$$

$$B_1 = r A_i \qquad B_2 = tt'r' A_i e^{i\delta} \qquad B_3 = tt'r'^3 A_i e^{2i\delta} \quad . \quad . \quad . \quad ,$$

where r is the reflection coefficient and t is the transmission coefficient for waves moving from medium n to n_f, and r' and t' are equivalent quantities for waves moving from n_f to n. The sum of all B_i's is an infinite geometric progression which results in A_r, given by,

$$A_r = \frac{(1 - e^{i\delta})\sqrt{R}}{1 - Re^{i\delta}} A_i \quad .$$

In a similar manner A_t can be represented by,

$$A_t = \frac{T}{1 - Re^{i\delta}} A_i \quad .$$

In both of these equations, the definitions of,

$$R \equiv r^2 = r'^2 \qquad T \equiv tt'$$

were used. R represents the fraction of the intensity reflected and T represents the

fraction of the intensity transmitted at each interface. These are the mirror reflectance and transmittance.

Given an incident intensity of $A_iA_i^*$, the reflected and transmitted intensities are given by,

$$\frac{I_r}{I_i} = \frac{A_rA_r^*}{A_iA_i^*} = \frac{4R\sin^2(\delta/2)}{(1-R)^2 + 4R\sin^2(\delta/2)} \quad , \quad \textit{and}$$

$$\frac{I_t}{I_i} = \frac{A_tA_t^*}{A_iA_i^*} = \frac{(1-R)^2}{(1-R)^2 + 4R\sin^2(\delta/2)} \quad .$$

According to the transmission equation, transmission is unity whenever,

$$\delta = \frac{4\pi nl\cos\theta}{\lambda} = 2m\pi \quad ,$$

where m equals any integer. Using the relation $c = \upsilon\lambda$, this equation becomes,

$$\nu_m = m\frac{c}{2nl\cos\theta} \quad .$$

This equation defines the maximum transmission frequency of the etalon and is again repeatable with m equal to any integer. By inverting this equation, it can be seen that any wavelength which is an integral divisor of the cavity spacing will be transmitted. This fact will be used in the tuning circuit that will be shown in Chapter 4.

If l and θ are fixed, the equation will represent the free spectral range, i.e. the separation between peaks in the transmission. Defining the free spectral range (FSR) as $\Delta\upsilon$, it can be expressed as,

$$\Delta \nu \equiv \nu_{m+1} - \nu_m = \frac{c}{2nl\cos\theta} \quad .$$

Given these equations, the theoretical transmission is illustrated in Figure 3.2 with various reflectivities. As is shown, the width of each band ($\Delta\upsilon_{1/2}$) will become more narrow as the reflectivity is increased. A useful relation is the ratio of the half-width to the FSR. This relation is call the finesse, and is defined as,

$$F \equiv \frac{\pi\sqrt{R}}{1 - R} = \frac{\Delta \nu}{\Delta \nu_{1/2}} \quad .$$

The finesse is typically used to measure the resolving power of the etalon. It should also be noted that finesse is also dependent on mirror flatness and the input angular beam spread. Although these effects will not be discussed here, a thorough discussion can be found in Hernandez[3].

The maximum transmission, MAX, of an etalon is limited by the absorption, *a*, and the reflectivity of the mirrors and is given by,

$$MAX = \left(1 - \frac{a}{(1 - R)}\right)^2 \quad .$$

Using modern optical coatings, *a* can be reduced to 0.15 %. A plot of the throughput versus reflectivity is shown in Figure 3.3. Etalons are the basic building block of interference filters, which are described in next section.

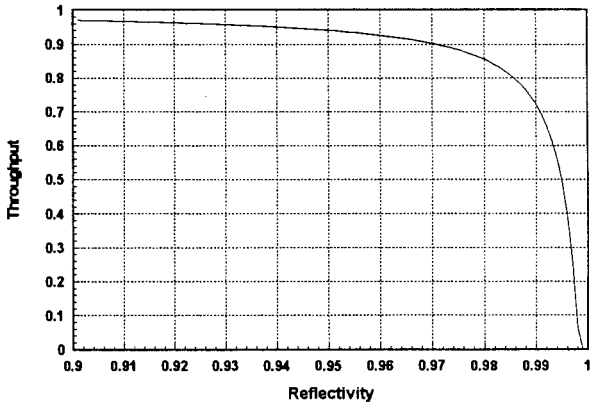

Figure 3.3 -- Throughput versus Reflectivity for a Fabry-Perot etalon

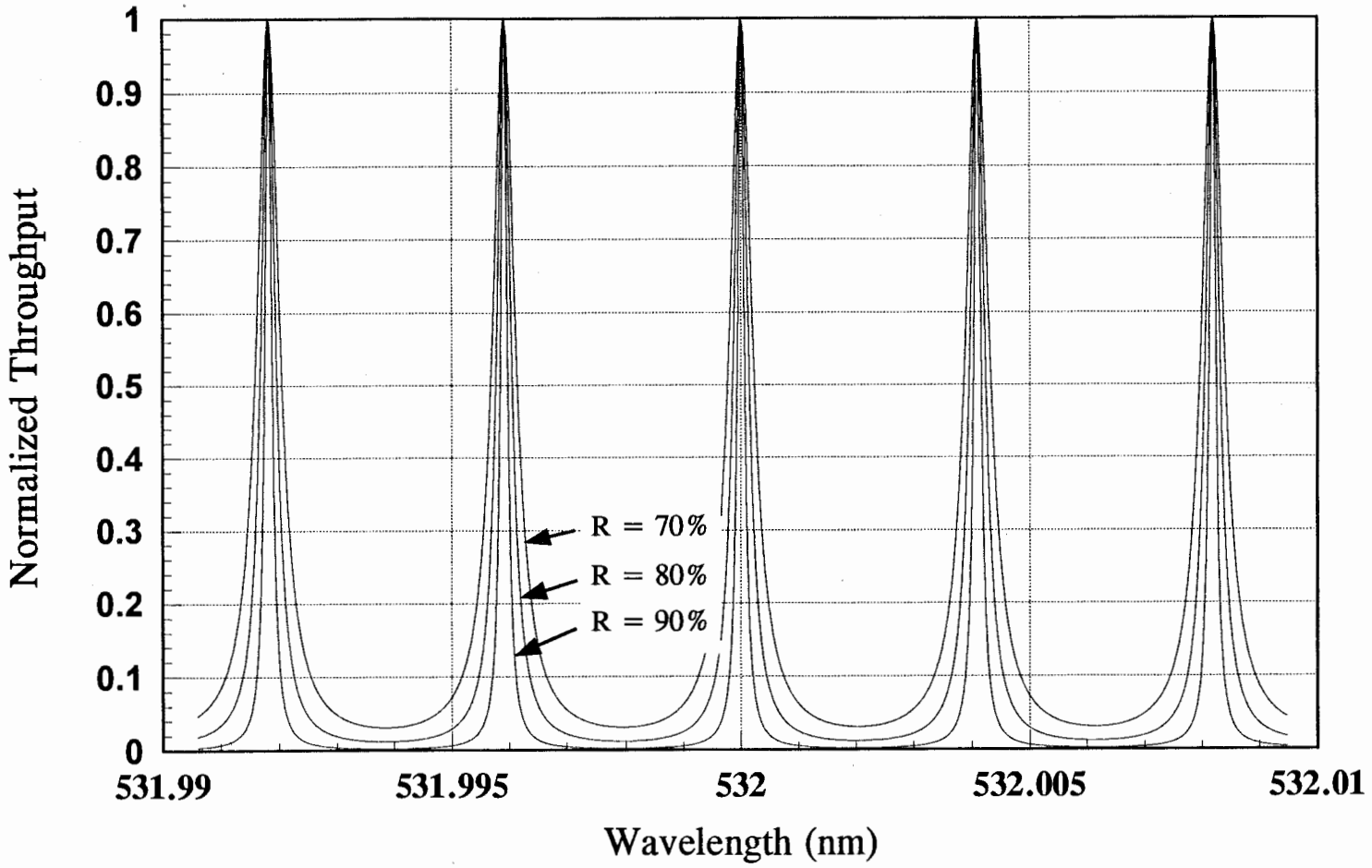

Figure 3.2 -- Etalon Passbands with Different Reflectivities

3.2. Interference Filters

Consider an etalon with a cavity of 266 nm. This low-order etalon would pass 532 nm, or any wavelength which is an integer divisor of 532 nm. This could be manufactured by depositing dielectric or metal layers onto a substrate forming an etalon[21].

A typical 3 cavity, 50 layer filter is shown in Figure 3.4. As is illustrated in the figure, there are three separate and distinct etalons in this filter each coupled by another dielectric layer. This layer can be made to filter out other unwanted passbands or to increase the rejection at other specific wavelengths. Figure 3.5 shows the combining effects of the 3 cavities[22]. Each additional cavity shapes and narrows the bandpass resulting in a flatter top and a more narrow bandpass. This is an idealized filter; for comparison, a measured 2 cavity filter transmission curve is shown in Figure 3.6.

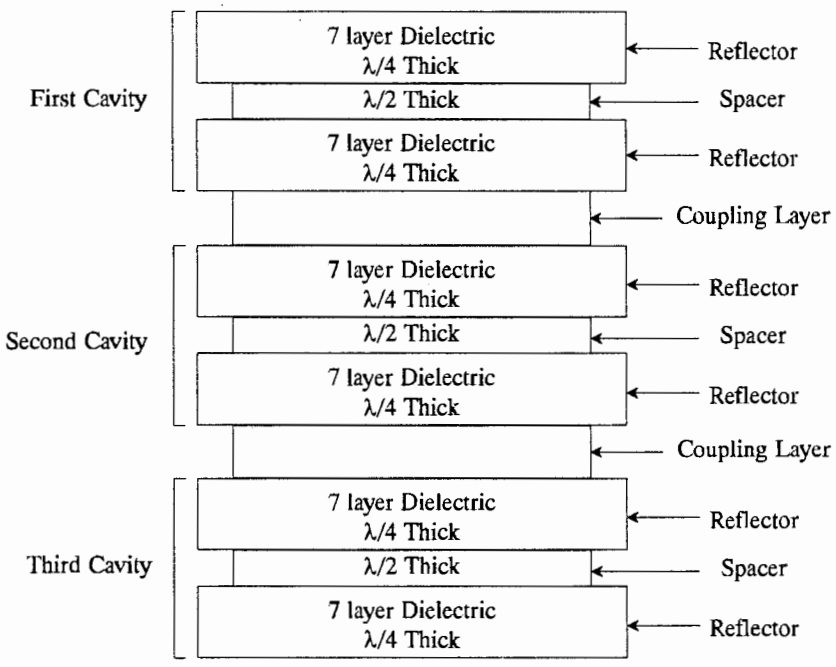

Figure 3.4 -- Typical 3 Cavity, 50 Layer Filter

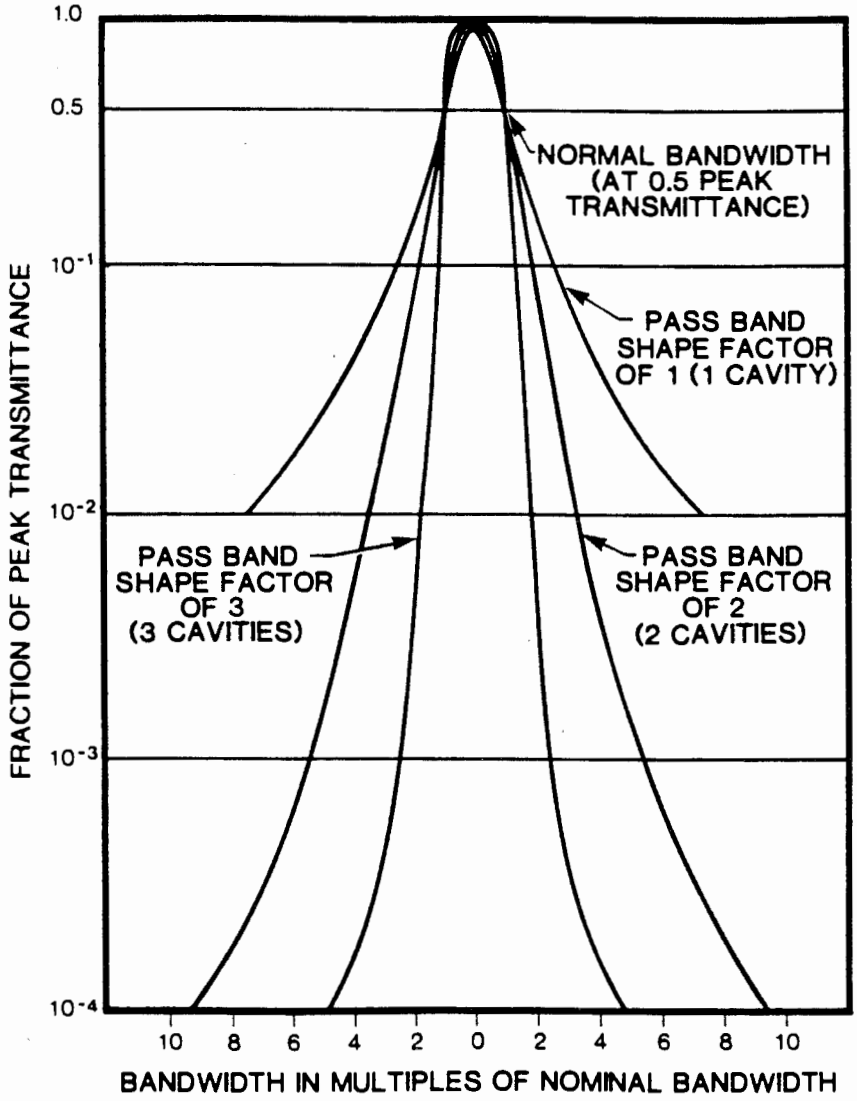

Figure 3.5 -- Effect of Multiple Cavities on Filter Bandpass
(After Oriel [22])

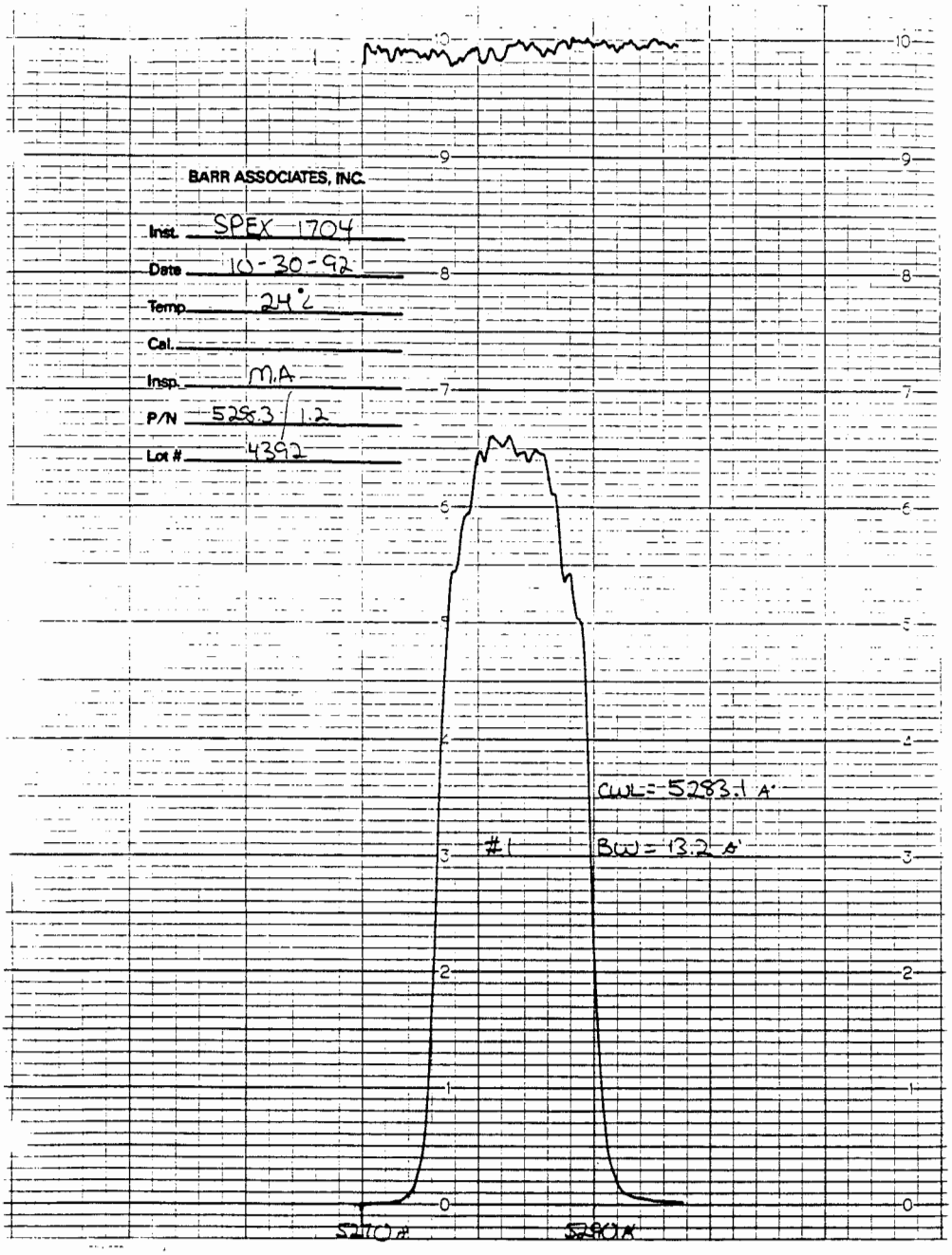

Figure 3.6 -- Measured Interference Filter Transmission

The Fabry-Perot interferometer and interference filters are critical for the daytime operation of the LAMP lidar system. In the next chapter, the application of these optical elements to the daytime performance is shown.

Chapter 4

Day-Sky Background Reduction

Daytime operation of the LAMP system imposes certain design considerations that are not required for nighttime operation. Specifically, high intensity background illumination over a wide spectral region, caused by diffuse scattering of sunlight, must be attenuated to keep the signal to noise ratio at an acceptable level. In this chapter, the optical system design factors that affect the background noise level are examined.

Some possible approaches that can be used to reduce the background are:

1) reduce the aperture of the telescope,
2) use a field stop to reduce the field of view of the telescope,
3) choose a wavelength that has a lower radiance value,
4) reduce the bandpass of the optical filter in the detector channel,
5) minimize stray light paths by using better baffle techniques for the telescope and detector box.

The first alternative is not practical, since a smaller aperture telescope also reduces the desired signal in the same proportion as the background. The second, implemented with an iris, is an effective method to reduce the background signal; however, the reduction in the field of view is limited by the laser beam divergence, the mechanical stability with which the beam is maintained in the telescope field, and by the near field form factor of the telescope. The third suggestion is not easily variable, since most high power pulsed lasers have a fixed frequency. However, since there is a large

difference in the radiance values over wavelength, use of available laser harmonics is the easiest way to move the wavelength to reduce background noise (i.e. tripled Nd:YAG). The fourth technique, reducing the bandpass of the input filter to approach the bandwidth of the laser, is effective provided that the filter can be matched to the laser wavelength in a stable manner. The last technique is a system design parameter affecting all measurements. The discovered stray light paths are blocked when strong signals cause spilling between detector channels during nighttime operation, but stray light effects are more pronounced and difficult to correct during daytime operation. To reduce this effect, the LAMP system has been equipped with blocking rings and telescope baffelling as part of the daytime design.

4.1. Telescope Field Stop

The first effective method for day-sky background reduction is the use of a telescope field stop. The position of the field stop is shown in Figure 4.1. This configuration was used before a fiber optic was put in place. Using Lowtran 7 radiance results, the predicted counts can be calculated by,

$$N(z) = \left[\frac{N * A_o * \varepsilon(\lambda) * T_D * S_{bw}}{E_p}\right] * \tau_d \quad ,$$

where N is the background radiance, A_o is the telescope area, $\varepsilon(\lambda)$ is the detector efficiency at wavelength λ, T_D is the f.o.v. of the telescope in sr, S_{bw} is the system bandwidth, E_p is the energy of one photon at the wavelength λ, and τ_d is the time of one range bin. T_D is determined from the iris size by the following relation,

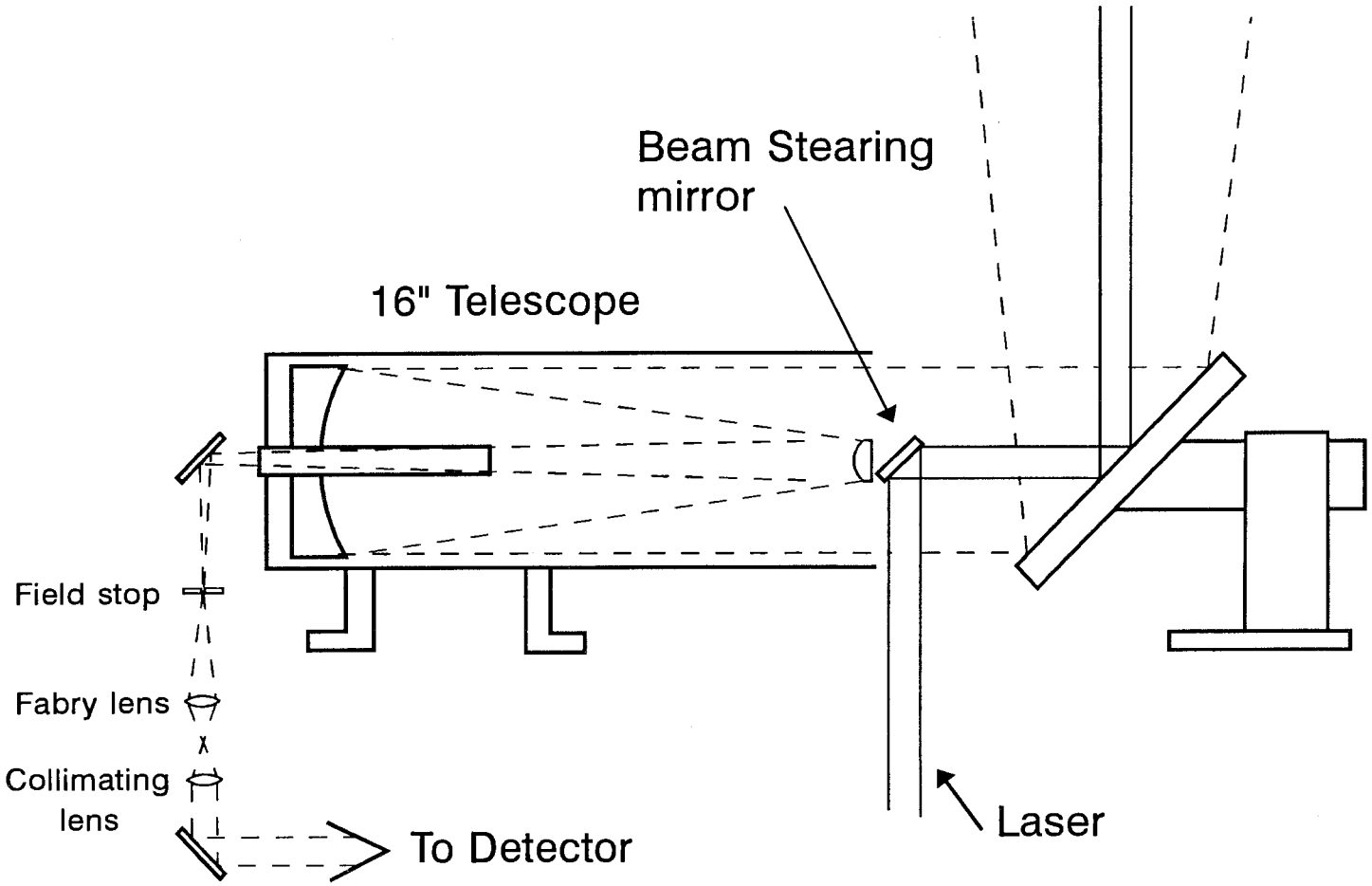

Figure 4.1 -- Drawing of the optical ray path through the receiver system. The position of the field stop and following two beam forming lenses is shown with respect to the 16" Cassegrain telescope and 24" collecting flat.

$$T_D = \pi \sin^2\left(\frac{FS}{2 * FL}\right) \quad ,$$

where *FS* is the field stop (iris size) and *FL* is the focal length of the telescope. Using these relationships, the background counts can be estimated. For iris sizes of 12.7 mm, 6 mm, 4 mm, 2 mm, and 1 mm, the expected counts on the 532 nm channel (0.3 nm bandwidth filter), with a 60 degree solar zenith angle, and a 10 minute integration, the expected counts are 1.14×10^7, 2.55×10^6, 1.14×10^6, 2.84×10^5, and 7.10×10^4, respectively.

Measurements using the original configuration with the iris were taken on August 21, 1992 using 6.35 mm, 4 mm, 3.2 mm, and 2.4 mm apertures and resulted in background counts of 2.2×10^4, 7.2×10^3, 3.3×10^3, and 2.2×10^3, respectively. The factor of 50 difference from the predicted counts maybe due to many factors. These include: 1) the Lowtran radiance value is a model value assuming certain atmospheric conditions that may be different than the conditions at the time of measurement, 2) there is vignetting present in the detector box, and 3) the optics in the detector box may be orientated in such a manner as to reduce the return in one polarization plane, and 4) the photon counting efficiency of the system relative to the setting of the discriminators.

To avoid the effects of the detector box on the background measurements, a photodiode was placed behind the telescope to measure the effect of the iris on the transmitted intensity. The resulting data as measured behind the telescope are shown in Figure 4.2. As can be seen from the figure, the background power increases as the square of the iris size or linear with the area. Converting these results to radiance, which

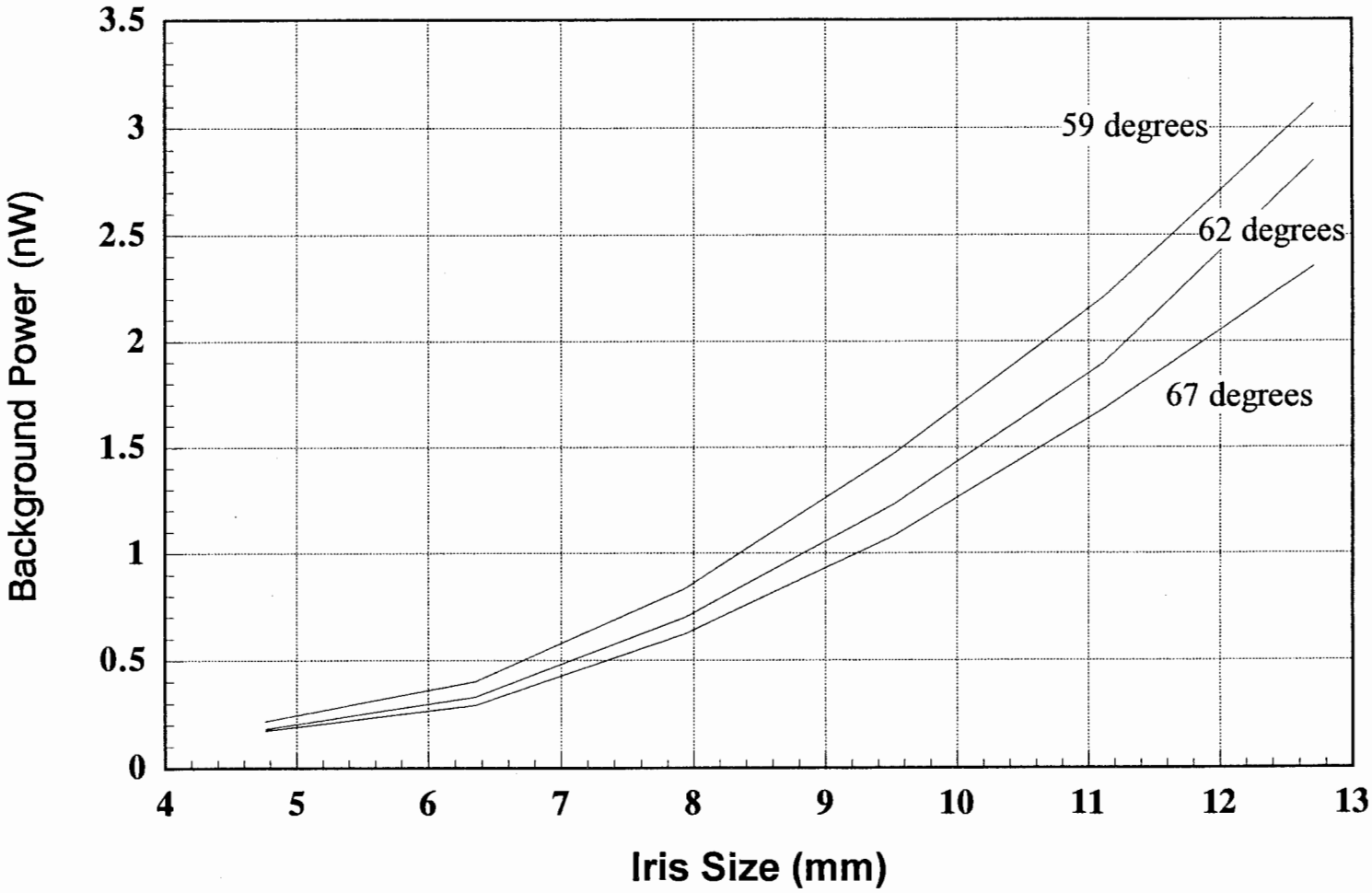

Figure 4.2 -- Measured Background Power at Three Solar Zenith Angles on November 13, 1992

were shown in Figure 2.8, the measured values and the Lowtran simulated values, as shown in Figure 2.6, are very close (differing by only 10 percent). Obviously, since the background is constant and the received power is reduced, the iris is an effective means to reduce the day-sky background signal. Ideally, the signal power will not be affected by the addition of the iris. This is not true since low altitude (near field) returns actually focus below the infinity focal point of the telescope. This geometry, with the telescope represented by a lens, is illustrated in Figure 4.3. Looking at the infinity focal point

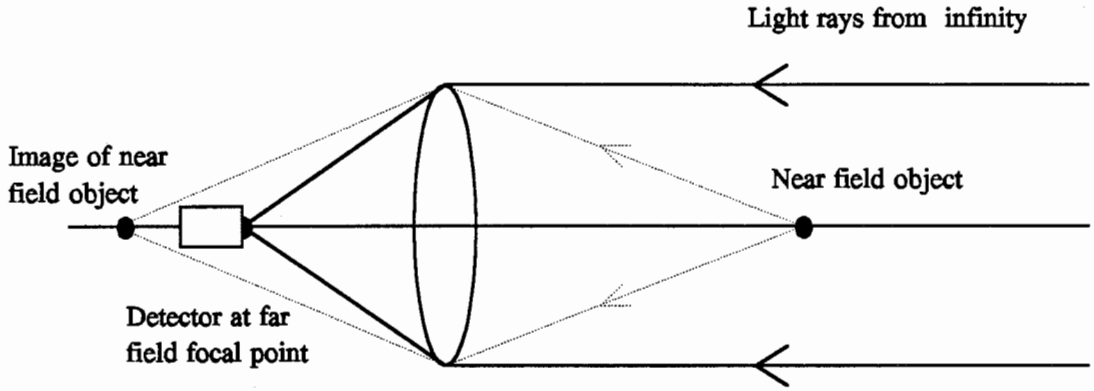

Figure 4.3 -- Image Point of a Near Field Object by a Telescope Focused at Infinity

plane, the spot size for different altitudes is shown in Figure 4.4. As is expected, the spot size at the infinity focal plane of a near field object will become larger than the iris. This results in an attenuated low altitude return.

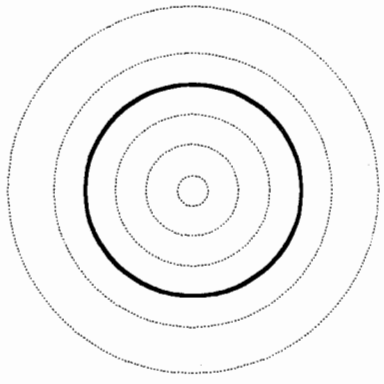

Figure 4.4 -- Image Size from Return at Different Altitudes (small circle is infinity return)

As the iris size becomes

smaller, the telescope f.o.v. will become less than the laser divergence thereby reducing the return signal even at the higher altitudes. Additionally, a smaller iris size can make the system more vibration sensitive. This occurs because vibrations cause the laser beam to wander in the f.o.v. of the telescope. It should be noted that the LAMP system has been outfit with a 1 mm fiber link from the telescope to the detector box. This sets an effective aperture of 1 mm limiting the f.o.v. of the telescope a half angle of 8.33×10^{-5}, solid angle of $2.18 * 10^{-8}$ sr, assuming a focal length of 6 meters. With the addition of a focal length reducing lens, this figure will change appropriately.

4.2. Optical System Bandwidth

The second effective method to decrease the background signal is to reduce the optical system bandwidth to block more of the solar spectrum. The filtering elements must be centered around the laser wavelength and be able to accommodate variations in laser frequency, so that the return signal is not attenuated. This is easier when the laser uses an injection seeder to maintain a stable frequency and a narrow linewidth output, as in the LAMP system. Two filtering element types have been used. These are the narrowband interference filter and the Fabry-Perot interferometer (both elements were discussed in Chapter 3). The implementation in the system will now be described.

4.2.1. Optical Element Layout

All detected wavelengths in the detector box have filters present. These filters reject out of band signals during nighttime operation and block solar radiation during the day. The nitrogen and water vapor Raman channels have 0.3 nm FWHM filters and the 355 nm channels have a 1.0 nm filter.

The optical filtering for the 532 nm detector section is shown in Figure 4.5. The return signal, containing all wavelengths, is incident on a beamsplitter (4). All wavelengths except 532 nm are transmitted, while 532 nm is reflected and passed through the Fabry-Perot etalon (5). The 532 nm return is unaffected by a hot mirror (6), and is filtered by the narrowband filter (7). The 532 nm signal is recorded by the low altitude (A/D) and high altitude (photon counting) channels. The narrowband filter (7) is thermally stabilized at 34°C and has a bandpass of 0.3 nm. Thermal stabilization is required because the filter's cavities would change size proportionally to temperature which would alter the center wavelength by 0.025 nm /°C.

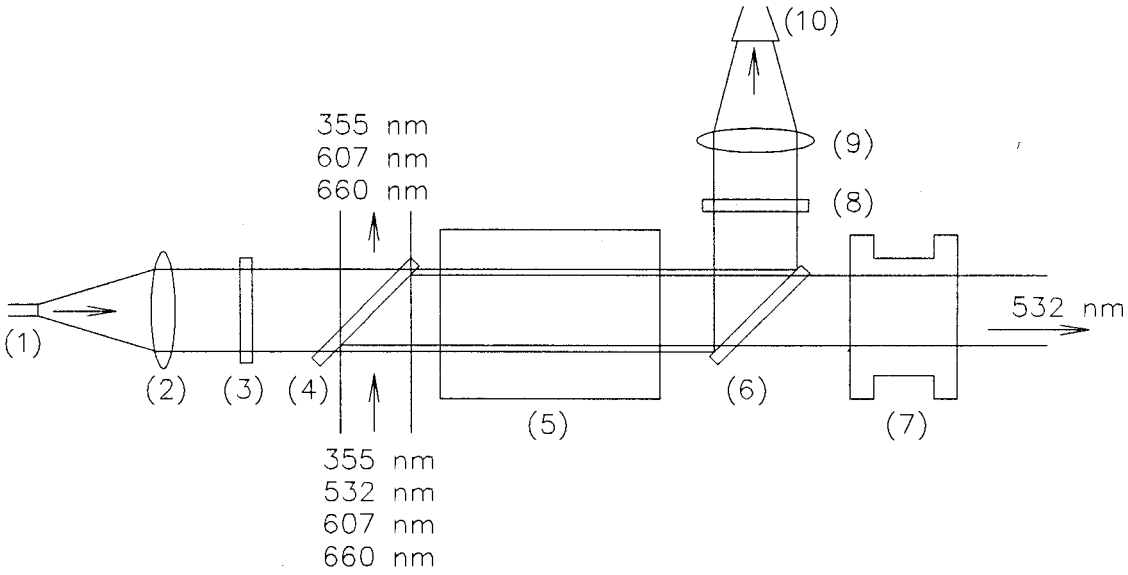

Figure 4.5 -- Optical Filtering for 532 nm Detector Section

The etalon is placed in the system when further background reduction is required (i.e. measurements while the solar zenith angle is low and the high altitude PMT's are on). The etalon has a bandpass of 0.01 nm. Three piezoelectric driver elements are used to tune the center wavelength of the etalon. The etalon plates are dual peak coated for

high reflectivity at 532 nm and 1064 nm. The 1064 nm coating allows the etalon to be tuned using the seed laser. Since 532 nm is an integer divisor of 1064 nm, tuning to the seed laser also maximizes transmission at 532 nm.

4.2.2. Optical Tuning Method of the Etalon

To tune the etalon, 10 percent of the 1064 nm seed laser for the Nd:YAG laser is injected into the detector box via a fiber at (1) as shown in Figure 4.5. The light is collimated to a 1" beam by a lens (2) followed by a narrowband interference filter (3) to remove flashlamp noise from the fiber output. The beam is unaffected by the beamsplitter (4), and passes to the Fabry-Perot etalon (5). The 1064 nm light is reflected by a hot mirror (6), and filtered again by an identical narrowband interference filter (8) to remove any lidar return light. Finally, the beam is focused by a lens (9) onto a Germanium photodiode (10) for detection. This system has the unique advantage of being able to optimize the etalon concurrently with operation of the lidar.

4.2.3. Tuning Circuit for the Etalon

The complete diagram, circuit description, and element table of the circuit are shown in Appendix A. This description will focus on the main operational subsystems of the circuit and some of the chip functions. Not all chips and connections will be discussed.

4.2.4. Measured Background Effect

Measurements of the background with the different filter bandwidths were carried out. The high altitude PMT's could not be operated at low solar zenith angles without the etalon in place, as a result, measurements were made with the low altitude PMT's by

simply comparing the digitized count totals. These counts should not change from one run to the next, thus providing an accurate comparison. The background was reduced by a factor of seven by the use of the etalon. Unfortunately, there is also a factor of four signal reduction due to the losses in the etalon. At the time the measurements were taken, the etalon coatings had deteriorated due to water absorption. New coatings have been received and those show only a factor of two loss. This demonstrates the effectiveness of narrowing the system filtering bandwidth.

4.3. Laser Harmonics

Referring again to the Lowtran irradiance and radiance curves, Figures 2.3 and 2.6, it is obvious that using a laser with a wavelength in or near a solar blind region can significantly reduce the received background. This section will show background and signal calculations for the three laser harmonic wavelengths, 532 nm, 355 nm, and 266 nm, as well as the vibrational Raman shifted wavelengths for nitrogen and water vapor for all of the harmonics. It will also be demonstrated that 266 nm is the best wavelength for daytime water vapor detection.

The calculations, which were done in Mathcad, for the signal and background counts received over a 30 minute integration are given in Appendix B. A full set of calculations are shown in the appendix for 532 nm molecular and Raman shifted returns for 532 nm, while only the results are given for 355 nm and 266 nm.

4.3.1. Frequency Doubled (532 nm)

The frequency doubled molecular scatter return can easily be detected relative to the daysky background on the digitizing channels. In fact, returns have been detected up

to 50 km during daytime operation. The detection problem encountered is with the inelastic (Raman) scattering.

The difficulty is due to the small cross section of the Raman scattering which is typically three orders of magnitude less than the molecular scattering of the same species. The small scattering cross section causes the backscattered signal to be well below the day-sky radiance values for minor species such as water vapor, 660 nm. The nitrogen channel, however, is able to receive returns during the day due to the number density of nitrogen. The results showing background counts and plots of the signal are shown in Appendix B immediately following the 532 nm calculation.

An additional difficulty encountered is the photon counting limitation of the PMTs used in the Raman channels. These PMTs will saturate when exposed to the day-sky background at solar zenith angles less than approximately 45 degrees for nitrogen (607 nm) and 80 degrees for water vapor (660 nm).

4.3.2. Frequency Tripled (355 nm)

The frequency tripled output has the same difficulties as the doubled output. The molecular scattering signal is detectable during the day, however the Raman scattered returns are not. The day-sky background is larger than the expected signal at both nitrogen and water vapor wavelengths (387 nm and 407.9 nm). It should be noted that the signal counts for water vapor are highest using 355 nm as the transmitted wavelength due to the larger cross section of the molecules. Results of the calculations are given in Appendix B for all cases from 355 nm.

4.3.3. Frequency Quadrupled (266 nm)

The frequency quadrupled output shows the best overall results for daytime measurements. The 266 nm wavelength is located in a solar blind region and therefore there are few background counts expected. In addition, the nitrogen Raman return and the water vapor Raman return are in a very low background area near the edge of the solar blind region. This allows all measurements to be made regardless of solar zenith angle provided the filtering system has enough blocking to remove out of band energy. Overall analysis of the atmospheric absorption and solar blind regions shows an optimal wavelength to be between 260 nm and 262 nm[23]. The output of the quadrupled Nd:YAG is close to this optimum range.

One problem with the use of 266 nm for daytime measurements is the limited blocking available with filters used at this wavelength. Currently available state-of-the-art filters will give only 10^4 blocking resulting in bleedthrough of the molecular return as well as the daysky background. Careful design with beamsplitters, and possibly double filtering, will be necessary to implement the frequency quadrupled output.

It should also be noted that the 266 nm output is not optimum for nighttime measurements. Due to the low output power of the current laser at this wavelength, the small telescope area, and the increased atmospheric scattering and absorption, it is currently not possible to get data above about 3 km altitude. Returns from greater altitudes may be possible with a larger laser and telescope system.

4.4. Optimum Configuration

The calculations given in the previous three sections lead to several conclusions.

The telescope should have a large area to collect the signal return, but also have a small field of view if using a wavelength subject to solar background. Additionally, narrow band filters or etalons must be used to eliminate as much of the day-sky background as possible. The choice of a laser wavelength that is in or near a solar blind will be necessary for successful daytime measurements.

The LAMP system currently uses the Raman shift of the 532 nm output for nitrogen and water vapor returns. As a result, daytime water vapor measurements are virtually impossible with the current system. With the results of the calculations presented, the system is being upgraded to use the 266 nm output for daytime water vapor measurements. In the next chapter, data taken with the current LAMP system configuration is presented.

Chapter 5

Daytime Measurements

This chapter compares daytime nitrogen Raman measurements made with the LAMP lidar system to model calculations and presents other daytime measurements taken in different system configurations. Measurements have been made with variations in the field stop size, bandwidths on the 532 nm channels, and the fiber installed.

5.1. Daytime Raman Comparison

Using the calculations outlined in Chapter 4, the lidar equation model return is plotted with a nighttime dataset for comparison in Figure 5.1. Applying an 85 degree solar background, the model would reach a signal-to-noise ratio of 1 at 4.9 km while the measured data would reach the same point at about 4.5 km. Actual daytime data is plotted in Figure 5.2 and shows nitrogen returns as the sun rises over the horizon. This data shows the signal-to-noise falling to 1 at about 2.5 km at a solar zenith angle of 87 degrees. The difference of about a factor of fifty lower in return signal shown in Figure 5.2 results from the use of a fiberoptic link which replaced the beam forming optics. Applying similar calculations to the theoretical water vapor Raman returns, a signal-to-noise ratio of 1 occurs at 1.4 km. However, when the system was operated while the solar zenith angle was 87 degrees, the resulting data showed no appreciable water vapor signal above background.

5.2. Variations in Field Stop

Two plots showing varying iris size are shown in Figures 5.3 and 5.4. Figure 5.3

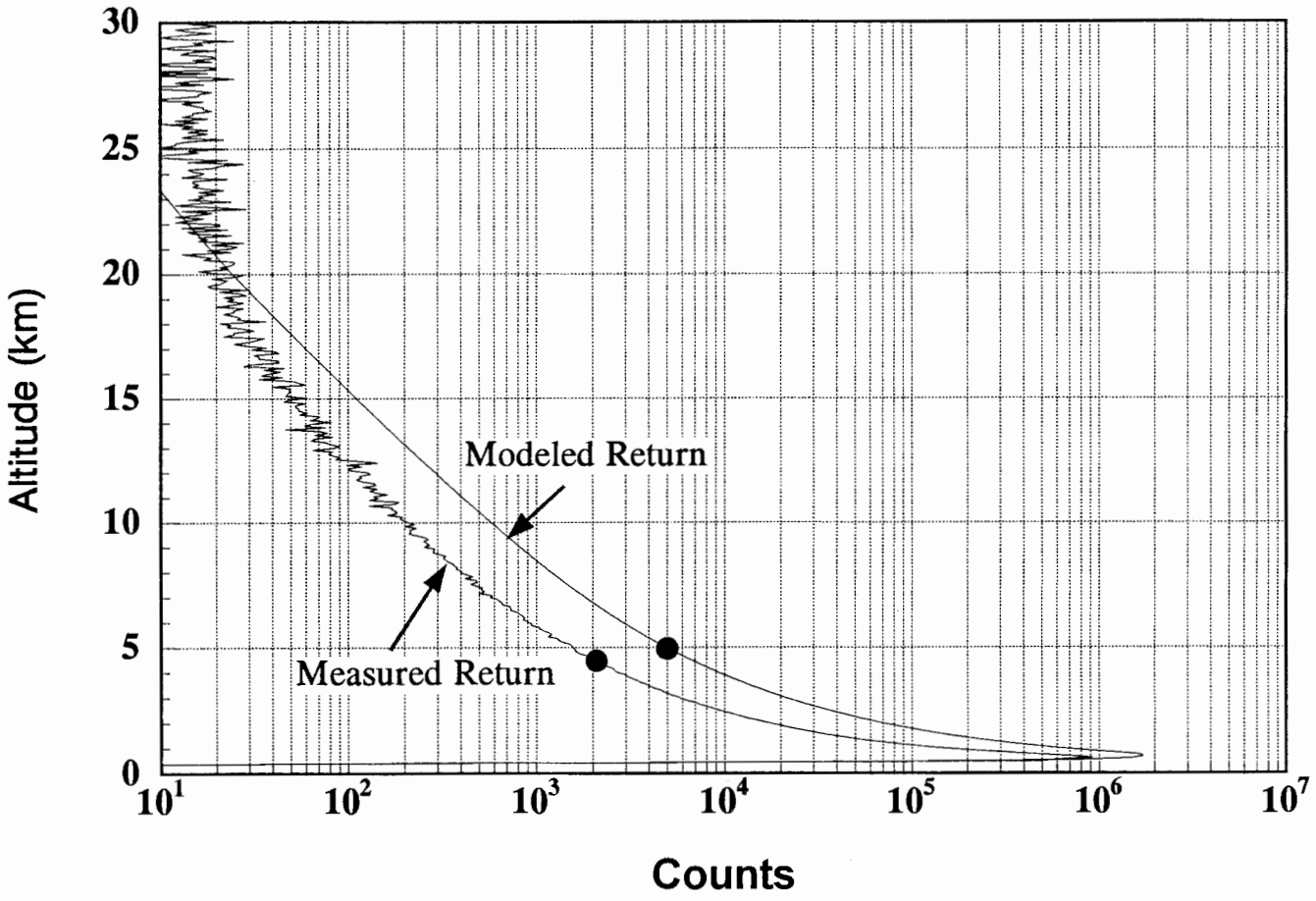

Figure 5.1-- Nighttime Raman Nitrogen Measured and Modeled Return
From October 24, 1992

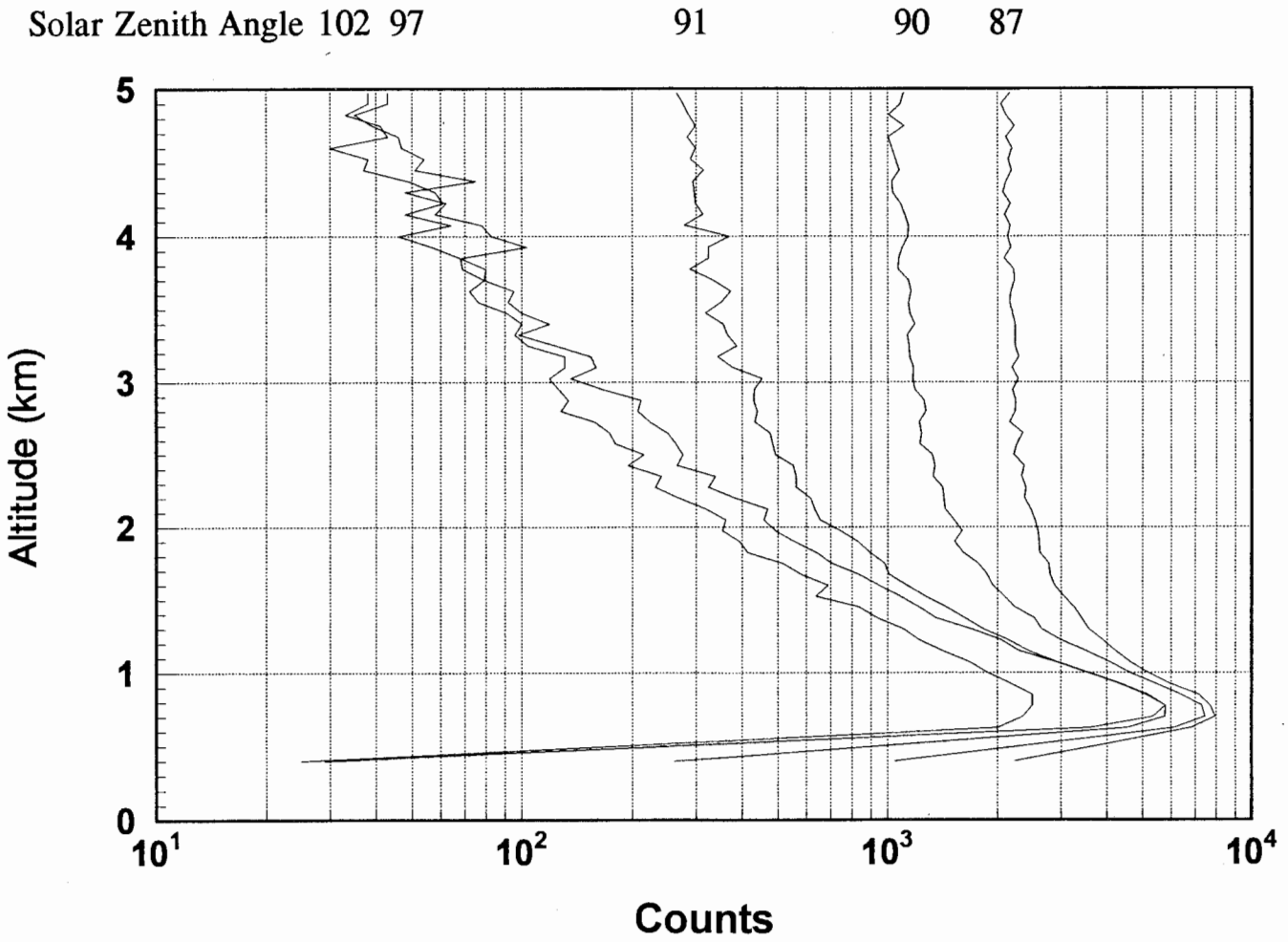

Figure 5.2-- Nitrogen Profiles as Sun Rises over Horizon
on January 21, 1993

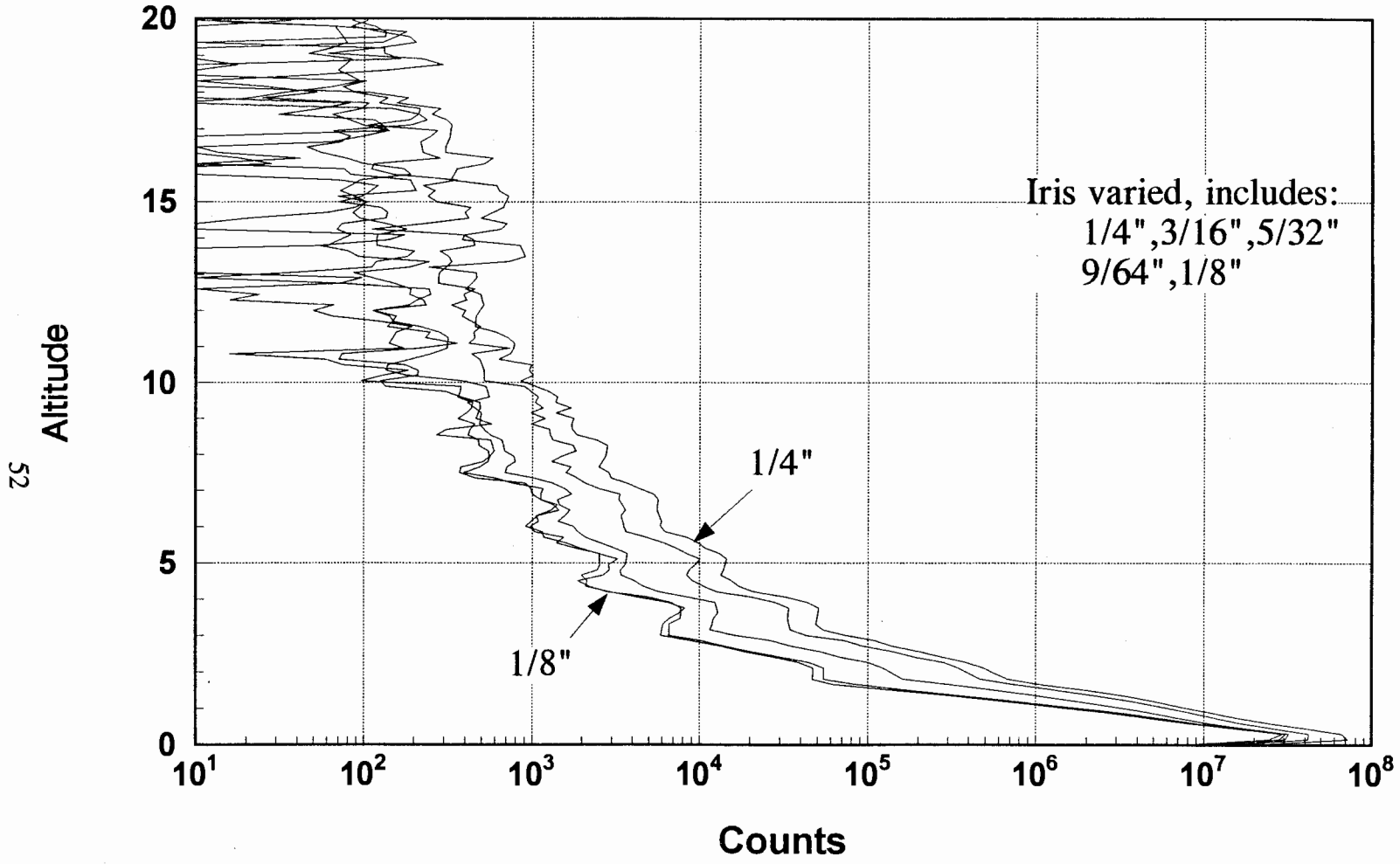

Figure 5.3-- Low Altitude Return with Iris Varied
from September 29, 1992

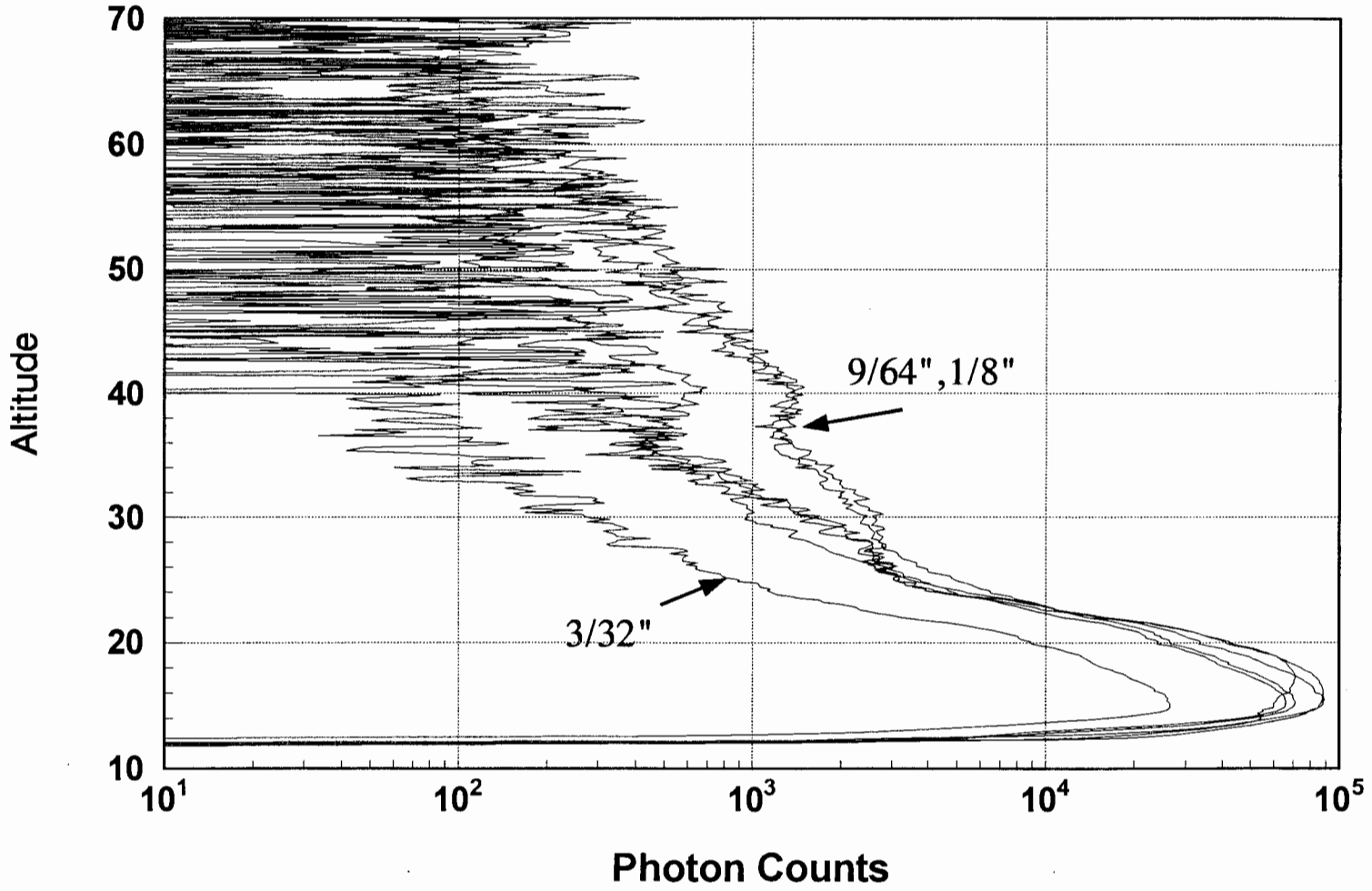

Figure 5.4-- High Altitude Return with Iris Varied
from August 21, 1992

shows the effect on the low altitude signal as the iris was varied. As seen in the figure, as the iris is dilated the signal-to-noise decreases slightly while the overall return becomes greater. The increase in the maximum low altitude signal is due to the iris blocking the low altitude return as discussed in Section 4.1. Figure 5.4 shows the high altitude data under the same conditions. This figure shows an optimum iris size of approximately 1/8" without an etalon. This results from several factors including, 1) beam mechanical vibration limits, 2) small aperture f.o.v. restrictions at the high altitudes, and 3) increase in day-sky background when the aperture is opened.

5.3. Variations in Filtering Bandwidth

The dependence of signal-to-noise on the filter bandwidths has been summarized in Figures 5.5 and 5.6. Figure 5.5 shows nighttime and daytime measurements taken with and without the etalon installed for low altitude using an aperture of 1/4". It is clear from this figure that the low altitude digitizing PMTs do not require the added etalon filtering under normal operating conditions since returns above background from almost 20 km were received in its absence and the PMT did not saturate. Figure 5.6 plots the nighttime data without the etalon and daytime data with the etalon using an aperture of 3/16". As previously stated, the high altitude PMTs require the etalon in place for mid to low solar zenith angles. The noticeable return attenuation from the etalon resulted from the deterioration of the etalon plate coatings due to the absorption of water. The change in altitude offset, up to 20 km at night, was done to prevent the PMT's from saturating due to the high return caused by the removal of the tripler (355 nm output).

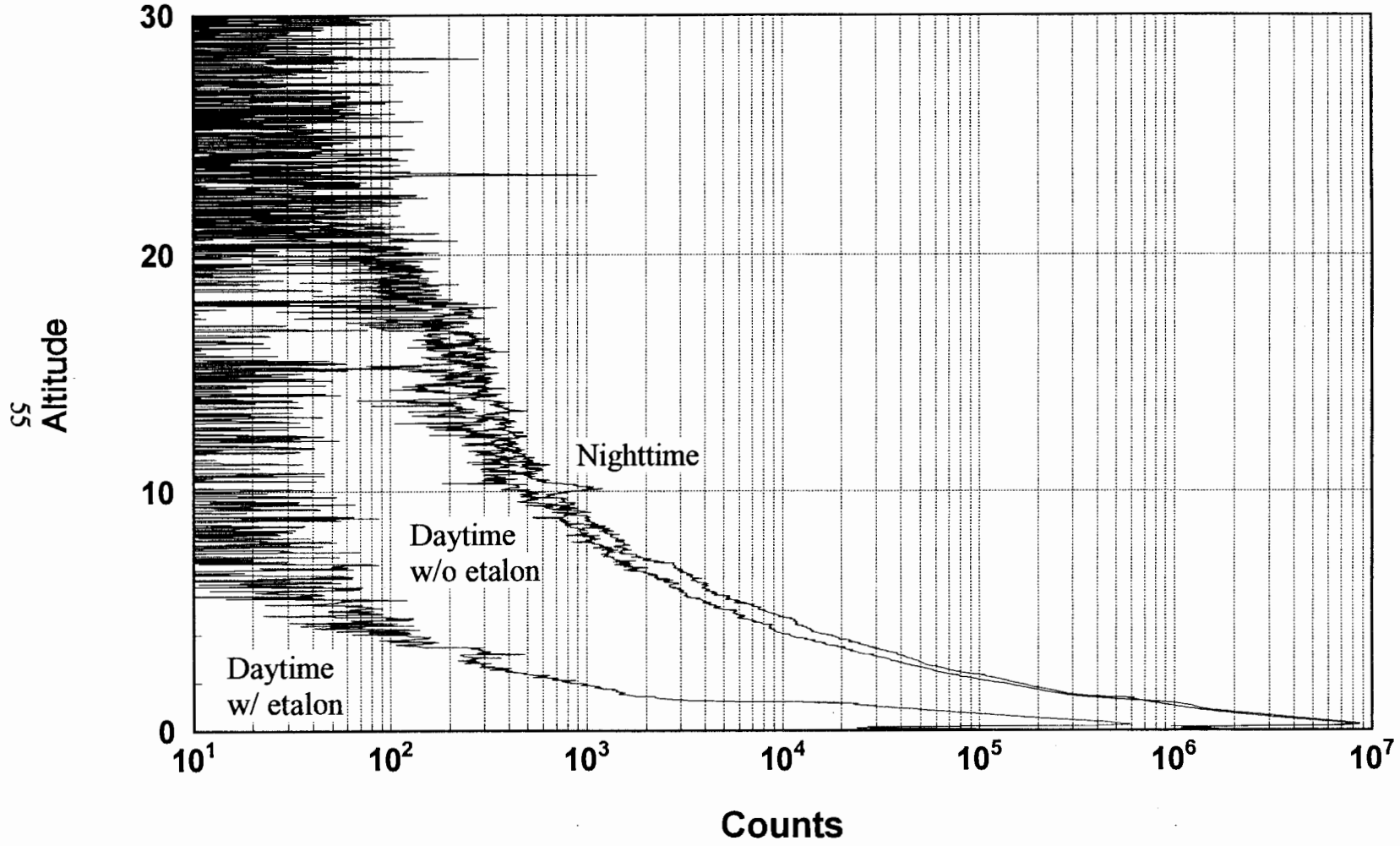

Figure 5.5-- Low Altitude Nighttime Data and Two Daytime Data with Different System Configurations from August 21, 1992

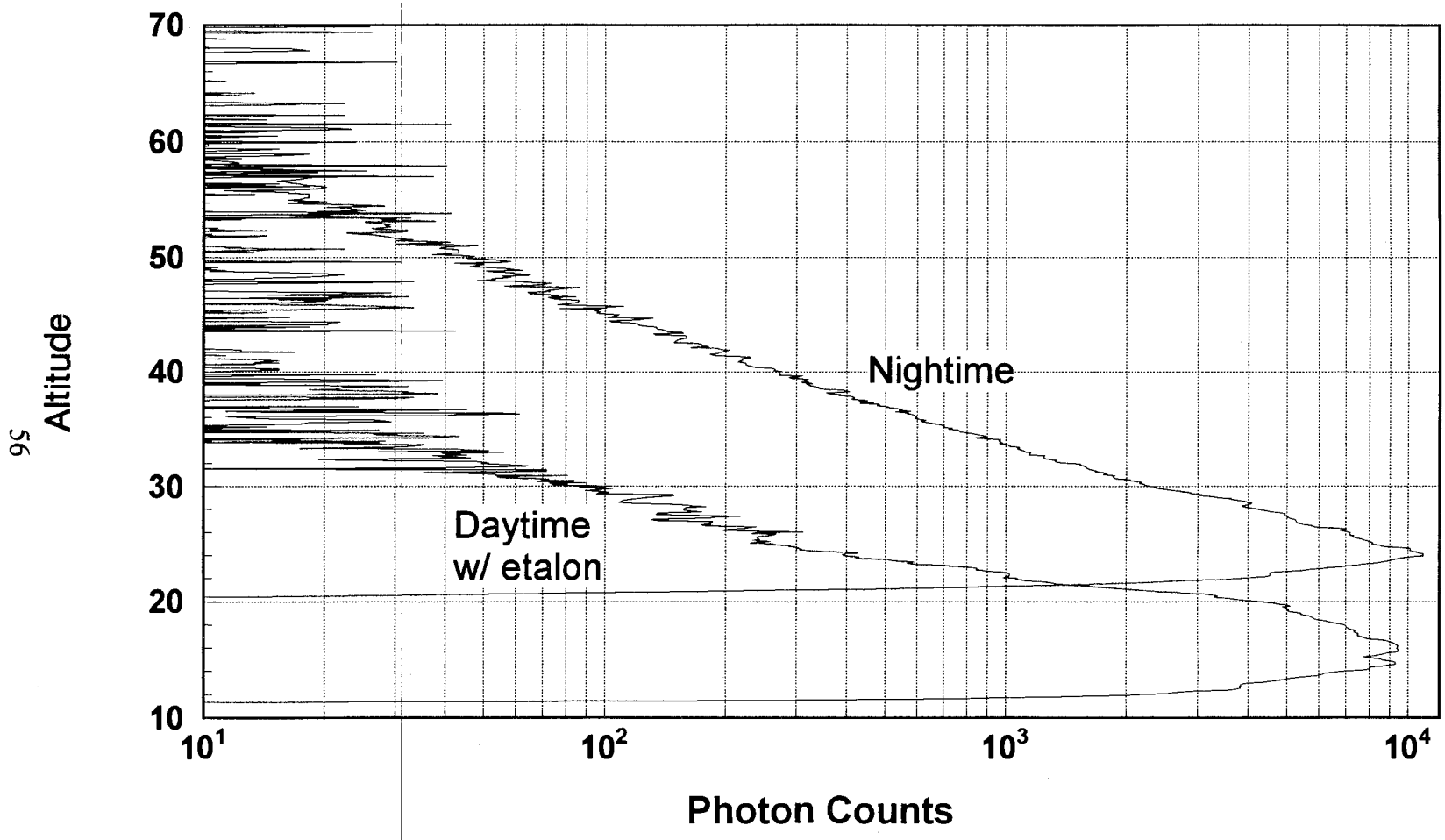

Figure 5.6 -- High Altitude Nighttime and Daytime Data Returns from August 21, 1992

5.4. Conclusion

Daytime measurements with lidar are important for monitoring layering processes and chemical reactions resulting from direct solar radiation. This thesis presented the basic operating concepts of lidar and the lidar equation in Chapter 1. Chapter 2 discussed the basic quantification and modeling of the solar background by Lowtran 7 and measured solar background values by the LAMP system. Fabry-Perot interferometers, or etalons, and interference filtering optics were introduced in Chapter 3.

Chapter 4 centered on day-sky background reduction techniques. These included, reducing the field of view of the telescope, using a laser harmonic near or in a solar blind region, and reducing the filtering bandpass of the optical system. The resulting "ideal" daytime system used an iris set at about 3/16", the fourth harmonic output, 266 nm, for Raman measurements of nitrogen and water vapor, and a 0.3 nm FWHM filter for the low altitude digitizing channels and a 0.01 nm FWHM etalon for the high altitude molecular return from 532 nm.

This chapter showed results from several different daytime runs of the LAMP system. Returns for the Raman channels were predicted and measured. The results showed that daytime measurements of nitrogen from 532 nm excitation is possible under certain conditions. However, while, theoretically, water vapor measurements are possible, the current system is not able to recover any usable signal. To allow daytime measurements, several future upgrades are proposed to improve the daytime performance of the LAMP system. These will be discussed in Chapter 6.

Chapter 6

Future Work

This chapter will present concepts that will be implemented to improve the daytime performance of the LAMP system. These include the use of polarization, shift of laser wavelength, and improvements to the etalon tuning system. In addition, a method to measure lower and middle atmospheric winds using the seed laser tuning technique will also be presented.

6.1. Polarization Day-sky Reduction Technique

The laser output is linearly polarized in one plane. This results in molecular and Raman scattering being polarized in the same direction. If a polarizer is included in the return path in the same plane as the return, the signal should not be affected. A plot of the day-sky degree of polarization is shown in Figure 6.1[24]. The polarization of the day-sky reaches a maximum at 90 degrees from the sun of about 90 percent. This would result in a 90 percent background reduction at zenith with a solar zenith angle of 90 degrees by the inclusion of a polarizer.

Several factors must be carefully planned including polarizing elements in the detector box, any positioning of mirrors that may have a favored polarization, laser output polarization orientation, and day-sky polarization direction. The detector box polarization will reduce overall return signal if it is not aligned with the laser polarization.

6.2. Laser Harmonics

As shown in Chapter 4, the 266 nm laser output provides many advantages over

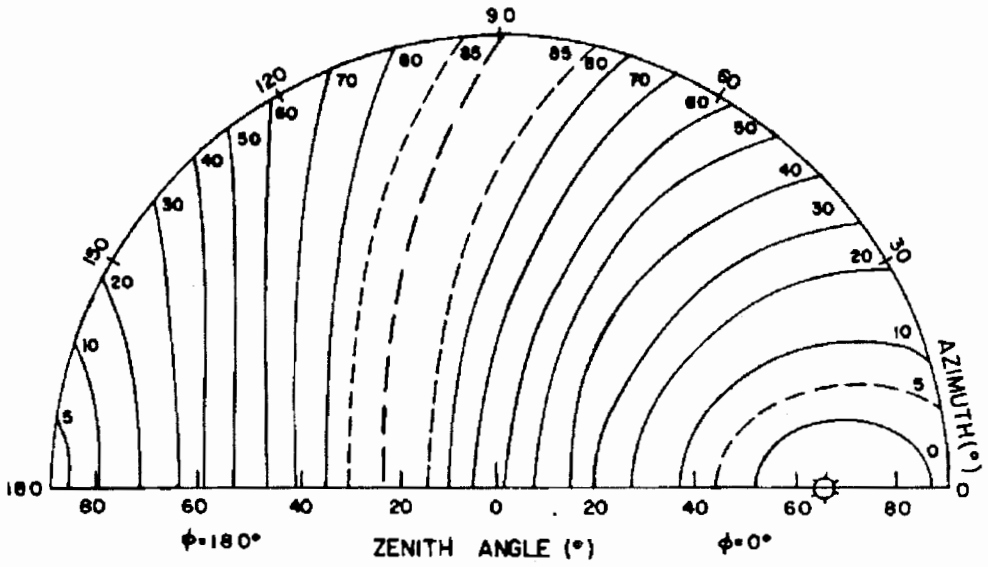

Figure 6.1 -- Degree of Day-sky Polarization (After Coulson [24])

the 532 nm wavelength in daytime operation. As a result, the use of the 266 nm output is being implemented in a system upgrade. This upgrade will include detectors for the 266 nm molecular as well as the nitrogen and water vapor returns. This upgrade is due to be completed by the end of the summer, 1993.

6.3. Finesse Optimization

The etalon tuning circuit discussed in Appendix A can be improved by the addition of a finesse optimization function. The etalon is tuned by three piezoelectric drivers attached to one of the plates. The circuit only optimizes the linear position of the plate by moving all three drivers simultaneously. Each driver is physically distinct and responds differently to the applied voltage. Finesse optimization is accomplished by moving each of the drivers independent of the others and finding the peak for each

position. The peak for each driver is locked in and after all drivers are scanned, the resulting position is the finesse optimized maximum transmission point.

6.4. Wind Measurements

Wind measurements with lidar require a stable filtering method. A technique has been developed to allow high resolution wind measurements using the etalon tuning method outlined in Chapter 4. A recently published paper on the wind sensor is given in Appendix C.

References

1. L. B. Elterman, "The measurements of stratospheric density distribution with the search light technique," J. Geophys. Res., 58, 519-530, 1953.

2. F. J. McClung and R. W. Hellwarth, "Giant optical pulsations from ruby," J. Appl. Phys., 33, pp.828-829, 1962.

3. R. M. Measures, Laser remote sensing. New York: John Weley & Sons, 1984.

4. C. R. Philbrick, D. B. Lysak, T. D. Stevens, P. A. T. Haris, and Y. -C. Rau, "Atmospheric measurements using the LAMP lidar during the LADIMAS campaign," Proceedings of the 16th International Laser Radar Conference, NASA Conference publications, no. 3158, pp. 651-654, 1992.

5. T. D. Stevens, P. A. T. Haris, Y. -C. Rau, C. R. Philbrick, "Latitudinal lidar mapping of stratospheric particle layers," accepted for publication in Adv. in Spac. Res., 1993.

6. L. L. Stowe, R. M. Carey, and P. P. Pellegrino, "Monitoring the Mt. Pinatubo aerosol layer with NOAA/11 AVHRR data," Geophysical Research Letters, vol. 19, no. 2, pp.150-162, 1990.

7. A. T. Young, "Rayleigh scattering," Applied Optics, vol. 20, no.4, pp. 533-535, 1981.

8. C. F. Bohren, D. R. Huffman, Absorption and scattering of light by small particles. New York: John Weley & Sons, 1983.

9. T. D. Stevens, "An optical detection system for a Rayleigh/Raman Lidar," MS Thesis, The Pennsylvania State University, 1992.

10. C. R. Philbrick, "Safety plan for LAMP lidar," Applied Research Laboratory Report, 1992.

11. R. A. McClatchey, R. W. Fenn, J. E. A. Selby, F. E. Volz, J. S. Garing, "Optical properties of the atmosphere," AFCRL-71-0279, Environmental Research Paper 354, AD 726116, 1971.

12. G. Waldman, J. Wootton, Electro-Optical Systems Performance Modeling. Massachusetts: Artech House, Inc, 1993.

13. F. X. Kneizys et al., "Users Guide to LOWTRAN 7," AFGL-TR-88-0177, Environmental Research Paper 1010, 1988.

14. R. W. Boyd, Radiometry and Detection of Radiation. New York: John Weley & Sons, 1983.

15. H. C. van de Hulst, Multiple Light Scattering Vol. 2. New York: Academic Press, Inc., 1980.

16. M. D. Steven, "Standard distributions of clear sky radiance," Quart. J. R. Met. Soc., 103, 457-465, 1977.

17. P. A. T. Haris, "Performance analysis of the LAMP Rayleigh/Raman lidar system," MS Thesis, The Pennsylvania State University, 1992.

18. C. Fabry and A. Perot, "Sur les franges des lames minces argentees et leur application a la mesure de petites epasseurs d'air," Ann. Chim. Phys., vol. 12, pp. 459-501, 1897.

19. G. Hernandez, Fabry-Perot Interferometers. New York: Cambridge University Press, 1988.

20. A. Yariv, Optical Electronics. Philadelphia: Saunders College Publishing, 1991.

21. W. G. Driscoll Ed., W. Vaughan A. Ed, Handbook of Optics. New York: Mcgraw-Hill Book Company, 1978.

22. Oriel Corporation, Optics & Filters Catalog, Vol. 3, pp. 2-30, 1990.

23. D. Renaut, R. Capitini, "Boundary-layer water vapor probing with a solar-blind Raman lidar: validations, meteorological observations and prospects," Journal of Atmospheric and Oceanic Technology, 5, 585-601, 1988.

24. K. L. Coulson, Polarization and intensity of light in the atmosphere. Hampton: A. Deepak Publishing, 1988.

Appendix A

The circuit diagram, Figure A-1, and component list, Table A-1, follow the description. This description does not discuss all connections in the circuit, rather it is a functional discussion of the major components in the circuit. The description starts with the timing.

The timing subsystem controls the timing for all other subsystems. The master clock, chip 11, is a 2 MHz square wave generator. The clock pulses are blocked until a high is detected on the ***B*** input on chip 16. When the ***B*** input signal is low, the circuit is held at a non-functioning state with the last value held on the output to the Burleigh ramp generator. The circuit will begin operation when the ***B*** input is set high. Chip 12 divides the clock frequency by 2 and sends it to the sequential clock generator, chip 15. The sequential clock generator allows operations to occur in a certain order, and provides a dead time in between operations permitting device states to settle. The rest of the operational overview will be completed in the executed order.

The first operation is the analog to digital conversion of the voltage from the Germanium photodiode. The input from the photodiode is denoted by ***P*** on the diagram. The signal is converted to a digital signal by an 8-bit flash A/D converter, chip 21. The A/D converter requires two clock pulses to convert the data and put the result on the output buffer. The two clock signals are pins 1 and 3 on chip 15. The output data is on the buffer 50 ns after the second clock pulse.

After the data is placed on the output buffer of the A/D, the data is read by a comparator, chip 31. This comparator has an internal buffer containing data which is

compared to the data on the input data pins. Initially, the buffer is cleared and set to zero. If the value in the buffer is greater than the value on the data pins, nothing happens for the rest of the timing cycle. If the value in the buffer is less than the value on the data pins, the "less than" open collector output, pin 13, is pulled high. When the "less than" signal is detected, the new value on the data pins is loaded into the internal buffer of chip 31. Additionally, the output signal to the Burleigh ramp generator is saved as the maximum.

The output signal is created by the cascading of four 4-bit counters, chips 42, 44, 46, and 48. This 16-bit counter is fed into a 16-bit D/A, chip 51, creating a ramp function which is used to scan the etalon. When the save signal is given to the counters, chips 41, 43, 45, and 47, store the value of the respective counters. The last function of the first cycle is to increment the counters.

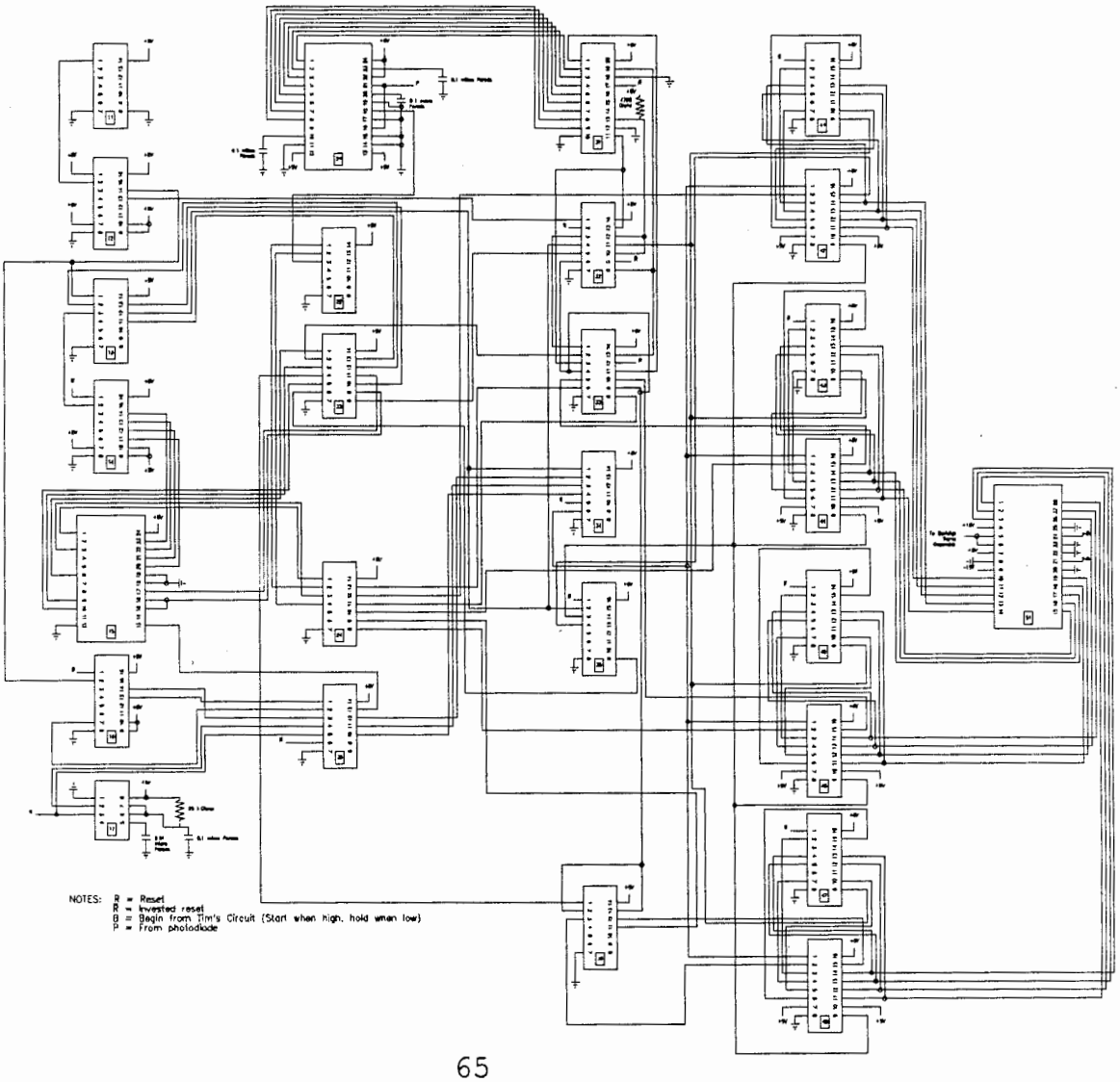
NOTES: R = Reset
R = Inverted reset
B = Begin from Tim's Circuit (Start when high, hold when low)
P = From photodiode

Table A-1

Chip Number	Component Description
11	TTLSWGM - 2 -- 2 MHz Square Wave Generator
12, 14, 42, 44, 46, 48	74HC161 -- 4-bit Synchronous Binary Counter with Asynchronous Clear
13, 32, 34,	74HC08 -- Quad 2-Input AND Gate
15	74HC154 -- 4-to-16 Line Decoder
16	74HC160 -- 4-bit Synchronous Decade Counter with Asynchronous Clear
17	LM555 -- Timer
21	CA3318CE -- 8-bit Flash A/D Converter
22, 33, 36	74HC32 -- Quad 2-Input OR Gate
23, 24, 25	74HC04 -- Hex Inverter
31	74F524 -- Internal Registered 8-bit Comparitor
35, 41, 43, 45, 47	74HC175 -- Quad D-Type Flip-Flop with Clear
51	AD7846KN -- 16-bit Voltage Output D/A Converter

Appendix B

This appendix presents the Mathcad files that were used to predict the system performance using certain models and assumptions. Values from the U.S. Standard atmosphere used included number density, n_t, nitrogen content, n_{N2}, and water vapor concentration, n_{H2O}. The subscripts denote the species at which the value applies and the additional subscript in the calculations denotes the altitude. The results from calculations done with Lowtran 7 shown in this thesis are used, i.e. atmospheric transmission, T, and radiance, R. The transmission has species, wavelength, and altitude subscripts, and radiance has species and wavelength subscripts.

The other constants or variables used are inputs or system values. These are listed in Table B-1. Following Table B-1 are calculations and results for the laser output wavelength of 532 nm, as well as the results from the same calculations using the 355 nm and 266 nm output. These results show the total background counts received in a 30 minute integration at wavelength L, and the total received counts as modeled by the lidar equation. The results are plotted for the molecular, Raman nitrogen, and Raman water vapor returns.

Table B-1

Variable Name	Description
L	Laser Output Wavelength in nm
z	Altitude (in km)
h	Planck's Constant
c	Speed of Light
E_L	Output Energy of the Laser at Wavelength L
λ_L	Wavelength
f	Frequency of Laser Output
N_P	Number of Photons Transmitted at Laser Wavelength L
λ_{Rx}	Wavelength of Vibrational Raman Return of Species x
$Tt_{x,y}$	Atmospheric Transmission at Wavelength x to Altitude y
$Tsx_{y,z}$	Atmospheric Transmission at the Scattered Raman Wavelength Shift of Species x from the Laser Wavelength y at Altitude z
σ_x	Backscattering Cross Section at Wavelength x
σ_{xy}	Raman Backscattering Cross Section of Species x from Laser Wavelength y
n_{xy}	Number Density of Species x at Altitude y (t is total density)
Δz	Integration Range Bin in Meters
ε_z	Telescope Geometric Form Factor
ε_{xy}	System Efficiency of Channel x from Scattered Wavelength y
FieldStop	Size of the Iris in Meters
FocalLength	Focal Length of Telescope in Meters
α	Spread of Telescope f.o.v.

Table B-1 (cont.)

Variable Name	Description
T_D	Telescope f.o.v. in sr
$Sx_{bw\,y}$	System Filtering Bandwidth of the Return from Species x from Laser Wavelength y
$R_{x\,y}$	Lowtran Radiance at a 60 degree Solar Zenith Angle at the Wavelength of the Return from Species x due to the Laser Wavelength y
$E_{p\,x\,y}$	Energy of a Scattered Photon from Species x from the Laser Wavelength y
$N_x(z)$	Number of Photons Received in One Range Bin for One Shot from Species x from Altitude z
B_x	Background Counts Received in One Range Bin for One Shot on Channel x
$Background_x(z)$	Background Counts for a Half Hour Integration on Channel x
$TotalCounts_x(z)$	Half Hour Integration of $N_x(z)$ on Channel x

Basic Constants and Definitions

$L := 532 \qquad z := 1,2..5 \qquad h := 6.6256 \cdot 10^{-34} \qquad c := 2.997925 \cdot 10^{8}$

$E_{532} := 0.6 \qquad E_{355} := 0.250 \qquad E_{266} := 0.100$

$\lambda_L := L \cdot 10^{-9} \qquad f := \frac{c}{\lambda_L} \qquad N_P := \frac{E_L \cdot \lambda_L}{h \cdot c}$

Raman Wavelength Shifts for Water Vapor and Nitrogen

$$\lambda_{RH2O} := \frac{1}{\left(-\frac{f}{c \cdot 100} - 3651.7\right) \cdot 100} \qquad \lambda_{RN2} := \frac{1}{\left(-\frac{f}{c \cdot 100} - 2330.7\right) \cdot 100}$$

Atmospheric Transmission from Lowtran 7

$Tt_{532,1} := 90.5 \quad Tt_{532,2} := 81.4 \quad Tt_{532,3} := 76.4 \quad Tt_{532,4} := 73.1 \quad Tt_{532,5} := 71.4$

$Ts_{N_{532,1}} := 92.0 \quad Ts_{N_{532,2}} := 84.2 \quad Ts_{N_{532,3}} := 80.0 \quad Ts_{N_{532,4}} := 77.2 \quad Ts_{N_{532,5}} := 75.8$

$Ts_{H_{532,1}} := 92.5 \quad Ts_{H_{532,2}} := 85.4 \quad Ts_{H_{532,3}} := 81.6 \quad Ts_{H_{532,4}} := 79.0 \quad Ts_{H_{532,5}} := 78.0$

$Tt_{355,1} := 83.7 \quad Tt_{355,2} := 68.5 \quad Tt_{355,3} := 60.0 \quad Tt_{355,4} := 54.1 \quad Tt_{355,5} := 50.6$

$Ts_{N_{355,1}} := 85.4 \quad Ts_{N_{355,2}} := 71.8 \quad Ts_{N_{355,3}} := 64.2 \quad Ts_{N_{355,4}} := 59.0 \quad Ts_{N_{355,5}} := 56.0$

$Ts_{H_{355,1}} := 86.4 \quad Ts_{H_{355,2}} := 73.5 \quad Ts_{H_{355,3}} := 66.5 \quad Ts_{H_{355,4}} := 61.6 \quad Ts_{H_{355,5}} := 58.8$

$Tt_{266,1} := 47.5 \quad Tt_{266,2} := 16.7 \quad Tt_{266,3} := 6.61 \quad Tt_{266,4} := 2.89 \quad Tt_{266,5} := 1.38$

$Ts_{N_{266,1}} := 68.1 \quad Ts_{N_{266,2}} := 41.3 \quad Ts_{N_{266,3}} := 27.5 \quad Ts_{N_{266,4}} := 19.4 \quad Ts_{N_{266,5}} := 14.4$

$Ts_{H_{266,1}} := 75.1 \quad Ts_{H_{266,2}} := 52.9 \quad Ts_{H_{266,3}} := 40.2 \quad Ts_{H_{266,4}} := 32.6 \quad Ts_{H_{266,5}} := 27.4$

Backscattering Cross Section from Measures

$\sigma_{532} := 6.22 \cdot 10^{-32} \qquad \sigma_{N2_{532}} := 5.642 \cdot 10^{-35} \qquad \sigma_{H2O_{532}} := 1.26 \cdot 10^{-34}$

$\sigma_{355} := 3.14 \cdot 10^{-31} \qquad \sigma_{N2_{355}} := 2.85 \cdot 10^{-34} \qquad \sigma_{H2O_{355}} := 6.34 \cdot 10^{-34}$

$\sigma_{266} := 9.96 \cdot 10^{-31} \qquad \sigma_{N2_{266}} := 6.45 \cdot 10^{-34} \qquad \sigma_{H2O_{266}} := 2.01 \cdot 10^{-33}$

Number Density from U.S. Standard (H2O from Mid. Lat.)

$n_{t_1} := 2.3113 \cdot 10^{25}$ $n_{N2_1} := 0.78 \cdot n_{t_1}$ $n_{H2O_1} := 1.3760 \cdot 10^{23}$

$n_{t_2} := 2.0928 \cdot 10^{25}$ $n_{N2_2} := 0.78 \cdot n_{t_2}$ $n_{H2O_2} := 9.5733 \cdot 10^{22}$

$n_{t_3} := 1.8905 \cdot 10^{25}$ $n_{N2_3} := 0.78 \cdot n_{t_3}$ $n_{H2O_3} := 6.5241 \cdot 10^{22}$

$n_{t_4} := 1.7036 \cdot 10^{25}$ $n_{N2_4} := 0.78 \cdot n_{t_4}$ $n_{H2O_4} := 3.4749 \cdot 10^{22}$

$n_{t_5} := 1.5312 \cdot 10^{25}$ $n_{N2_5} := 0.78 \cdot n_{t_5}$ $n_{H2O_5} := 2.3488 \cdot 10^{22}$

System Parameters

$\Delta z := 150$ $\varepsilon_z := 1$ $A_o := 0.1257$

System Efficiency

$\varepsilon_{532} := 1947 \cdot 10^{-5}$ $\varepsilon_{N2_{532}} := 943 \cdot 10^{-5}$ $\varepsilon_{H2O_{532}} := 328 \cdot 10^{-5}$

$\varepsilon_{355} := 717 \cdot 10^{-5}$ $\varepsilon_{N2_{355}} := 889 \cdot 10^{-5}$ $\varepsilon_{H2O_{355}} := 1061 \cdot 10^{-5}$

$\varepsilon_{266} := 441 \cdot 10^{-5}$ $\varepsilon_{N2_{266}} := 515 \cdot 10^{-5}$ $\varepsilon_{H2O_{266}} := 588 \cdot 10^{-5}$

Telescope Field of View

$FieldStop := 1 \cdot 10^{-3}$ $FocalLength := 6$ $\alpha := \frac{FieldStop}{2 \cdot FocalLength}$ $T_D := \pi \cdot \sin(\alpha)^2$

System Bandwidth

$S_{bw_{532}} := 0.3 \cdot 10^{-9}$ $SN2_{bw_{532}} := 0.3 \cdot 10^{-9}$ $SH2O_{bw_{532}} := 0.3 \cdot 10^{-9}$

$S_{bw_{355}} := 1 \cdot 10^{-9}$ $SN2_{bw_{355}} := 1 \cdot 10^{-9}$ $SH2O_{bw_{355}} := 1 \cdot 10^{-9}$

$S_{bw_{266}} := 6 \cdot 10^{-9}$ $SN2_{bw_{266}} := 6 \cdot 10^{-9}$ $SH2O_{bw_{266}} := 6 \cdot 10^{-9}$

Radiance from Lowtran 7 (60 degree solar zenith angle)

$R_{532} := 102.1$ $R_{N2_{532}} := 85.9$ $R_{H2O_{532}} := 74.6$

$R_{355} := 67.2$ $R_{N2_{355}} := 64.5$ $R_{H2O_{355}} := 96.6$

$R_{266} := 2.623 \cdot 10^{-37}$ $R_{N2_{266}} := 3.77 \cdot 10^{-21}$ $R_{H2O_{266}} := 2.15 \cdot 10^{-5}$

Energy of a Background Photon

$$E_{p_{532}} := 3.7337 \cdot 10^{-19} \qquad E_{pN2_{532}} := 3.2707 \cdot 10^{-19} \qquad E_{pH2O_{532}} := 3.0096 \cdot 10^{-19}$$

$$E_{p_{355}} := 5.5952 \cdot 10^{-19} \qquad E_{pN2_{355}} := 5.1323 \cdot 10^{-19} \qquad E_{pH2O_{355}} := 4.8804 \cdot 10^{-19}$$

$$E_{p_{266}} := 7.4673 \cdot 10^{-19} \qquad E_{pN2_{266}} := 7.0043 \cdot 10^{-19} \qquad E_{pH2O_{266}} := 6.7561 \cdot 10^{-19}$$

Lidar Equations

$$N(z) := N_P \cdot \left(\frac{Tt_{L,z}}{100}\right)^2 \cdot \left(\sigma_L \cdot n_{t_z} \cdot \Delta z\right) \cdot \left[\frac{\varepsilon_z \cdot A_o}{4 \cdot \pi \cdot (1000 \cdot z)^2}\right] \cdot \varepsilon_L$$

$$N_{N2}(z) := N_P \cdot \left(\frac{Tt_{L,z}}{100} \cdot \frac{Ts_{N_{L,z}}}{100}\right) \cdot \left(\sigma_{N2_L} \cdot n_{N2_z} \cdot \Delta z\right) \cdot \left[\frac{\varepsilon_z \cdot A_o}{4 \cdot \pi \cdot (1000 \cdot z)^2}\right] \cdot \varepsilon_{N2_L}$$

$$N_{H2O}(z) := N_P \cdot \left(\frac{Tt_{L,z}}{100} \cdot \frac{Ts_{H_{L,z}}}{100}\right) \cdot \left(\sigma_{H2O_L} \cdot n_{H2O_z} \cdot \Delta z\right) \cdot \left[\frac{\varepsilon_z \cdot A_o}{4 \cdot \pi \cdot (1000 \cdot z)^2}\right] \cdot \varepsilon_{H2O_L}$$

Background Equations

$$B := \left[\frac{R_L \cdot A_o \cdot \varepsilon_L \cdot T_D \cdot \left(S_{bw_L} \cdot 1 \cdot 10^6\right)}{E_{p_L}}\right] \cdot 500 \cdot 10^{-9}$$

$$B_{N2} := \left[\frac{R_{N2_L} \cdot A_o \cdot \varepsilon_{N2_L} \cdot T_D \cdot \left(SN2_{bw_L} \cdot 1 \cdot 10^6\right)}{E_{pN2_L}}\right] \cdot 500 \cdot 10^{-9}$$

$$B_{H2O} := \left[\frac{R_{H2O_L} \cdot A_o \cdot \varepsilon_{H2O_L} \cdot T_D \cdot \left(SH2O_{bw_L} \cdot 1 \cdot 10^6\right)}{E_{pH2O_L}}\right] \cdot 500 \cdot 10^{-9}$$

Results

$L = 532$ $B = 2.19011$ $B_{N2} = 1.01877$ $B_{H2O} = 0.33444$

$Background(z) := 20 \cdot 60 \cdot 30 \cdot B$

$Background(1) = 78844.00756$

$Background_{N2}(z) := 20 \cdot 60 \cdot 30 \cdot B_{N2}$

$Background_{N2}(1) = 36675.88166$

$Background_{H2O}(z) := 20 \cdot 60 \cdot 30 \cdot B_{H2O}$

$Background_{H2O}(1) = 12039.82876$

$TotalCounts(z) := 20 \cdot 60 \cdot 30 \cdot N(z)$

$TotalCounts_{N2}(z) := 20 \cdot 60 \cdot 30 \cdot N_{N2}(z)$

$TotalCounts_{H2O}(z) := 20 \cdot 60 \cdot 30 \cdot N_{H2O}(z)$

z	N(z)	TotalCounts(z)	$TotalCounts_{N2}(z)$	$TotalCounts_{H2O}(z)$
1	55276.86349	$1.98997 \cdot 10^9$	$6.93215 \cdot 10^5$	4132.27498
2	10122.93527	$3.64426 \cdot 10^8$	$1.29175 \cdot 10^5$	596.84893
3	3580.22898	$1.28888 \cdot 10^8$	46248.00191	162.12205
4	1661.39277	$5.98101 \cdot 10^7$	21645.00959	44.99324
5	911.7552	$3.28232 \cdot 10^7$	11940.83743	18.77065

Molecular Scattering Results

Background(1) = 78844.00756

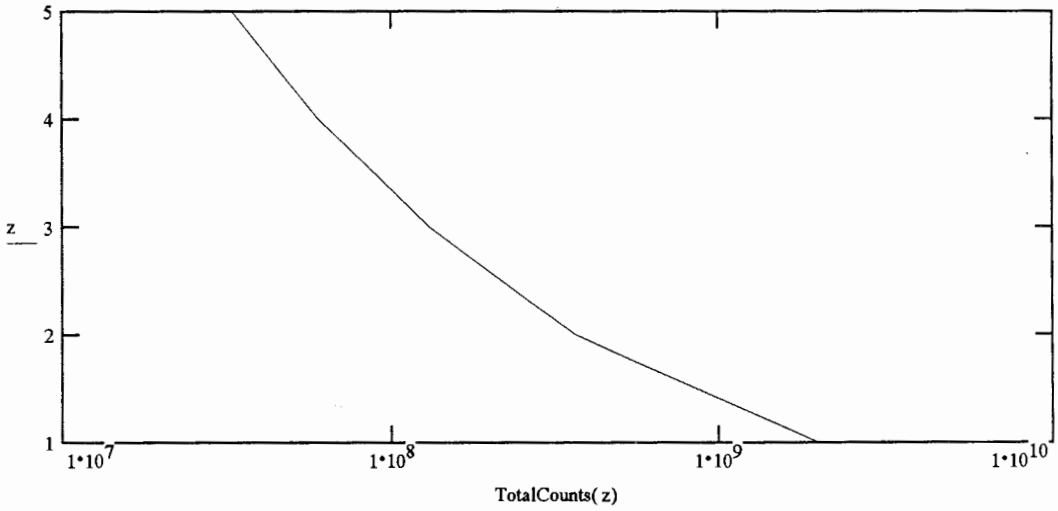

Results (cont.)

Raman Nitrogen Results

$\lambda_{RN2} = 6.07301 \cdot 10^{-7}$ Background $_{N2}(1) = 36675.88166$

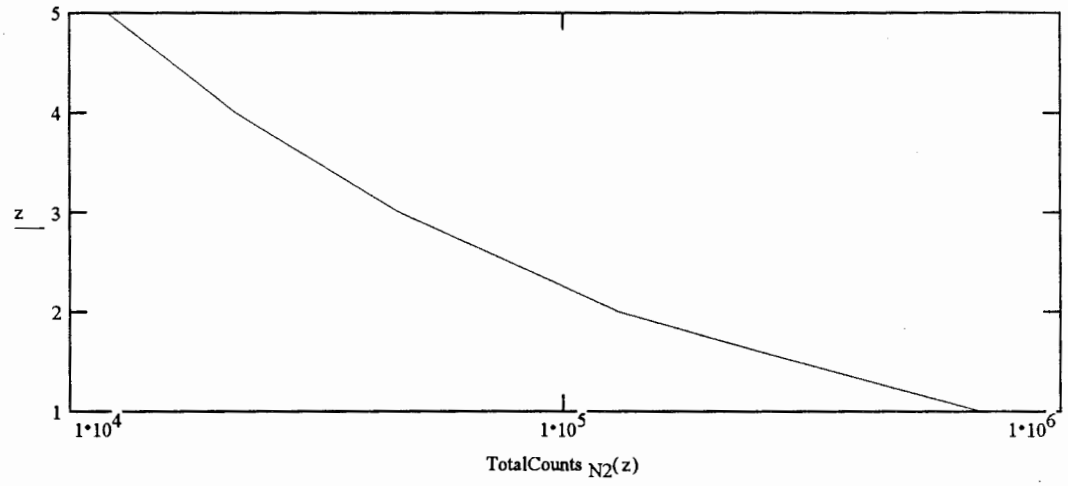

Raman Water Vapor Results

$\lambda_{RH2O} = 6.60271 \cdot 10^{-7}$ Background $_{H2O}(1) = 12039.82876$

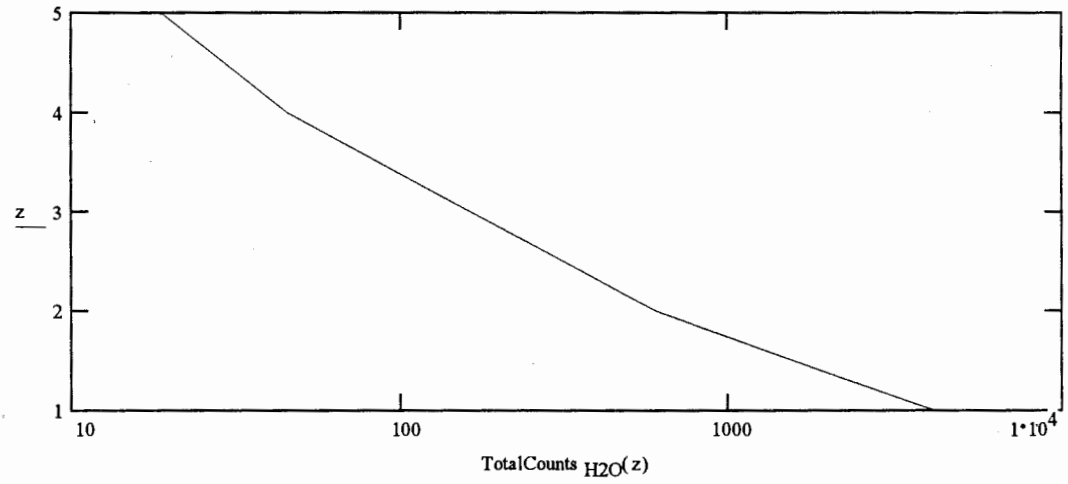

Results

$L = 355$ $B = 1.18077$ $B_{N2} = 1.53194$ $B_{H2O} = 2.87958$

$Background(z) := 20 \cdot 60 \cdot 30 \cdot B$ $Background_{N2}(z) := 20 \cdot 60 \cdot 30 \cdot B_{N2}$

$Background(1) = 42507.73614$ $Background_{N2}(1) = 55149.88404$

$Background_{H2O}(z) := 20 \cdot 60 \cdot 30 \cdot B_{H2O}$ $TotalCounts(z) := 20 \cdot 60 \cdot 30 \cdot N(z)$

$Background_{H2O}(1) = 1.03665 \cdot 10^5$ $TotalCounts_{N2}(z) := 20 \cdot 60 \cdot 30 \cdot N_{N2}(z)$

$TotalCounts_{H2O}(z) := 20 \cdot 60 \cdot 30 \cdot N_{H2O}(z)$

z	N(z)	TotalCounts(z)	$TotalCounts_{N2}(z)$	$TotalCounts_{H2O}(z)$
1	24439.65644	$8.79828 \cdot 10^8$	$7.87993 \cdot 10^5$	16154.88365
2	3705.41401	$1.33395 \cdot 10^8$	$1.22734 \cdot 10^5$	1956.25646
3	1141.36496	$4.10891 \cdot 10^7$	38592.52842	469.5666
4	470.35963	$1.69329 \cdot 10^7$	16209.87655	117.50234
5	236.69049	$8.52086 \cdot 10^6$	8277.76776	45.38163

Molecular Scattering Results

Background(1) = 42507.73614

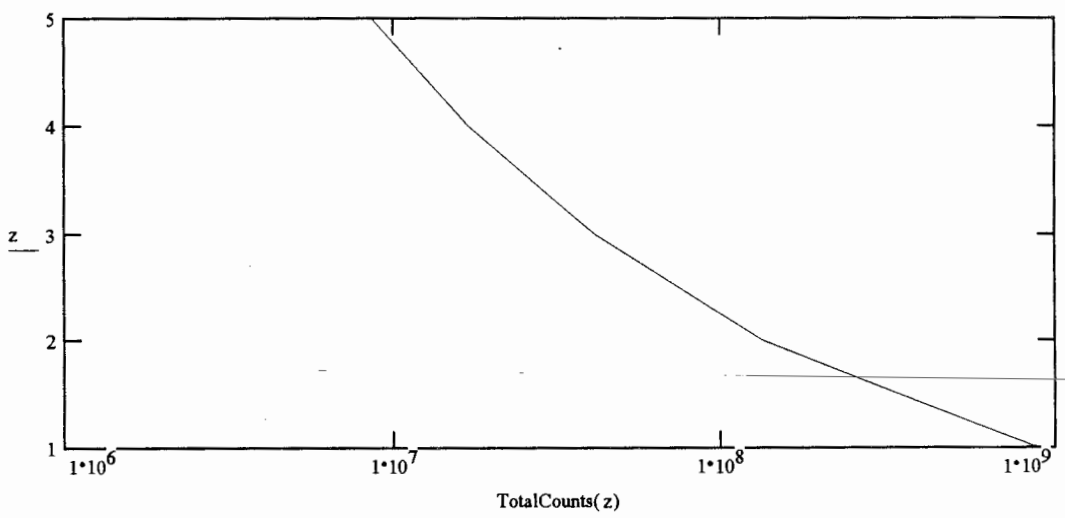

Results (cont.)

Raman Nitrogen Results

$\lambda_{RN2} = 3.87022 \cdot 10^{-7}$ Background $_{N2}(1) = 55149.88404$

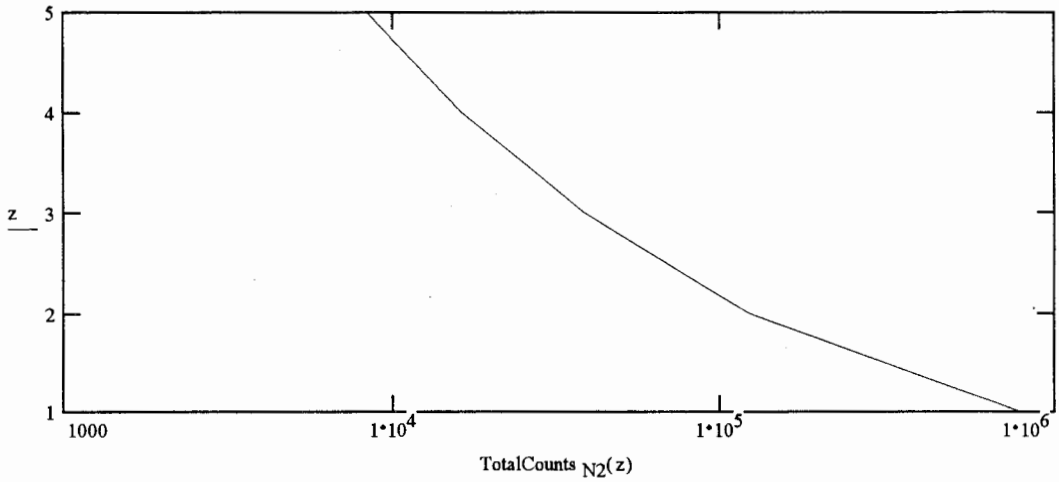

Raman Water Vapor Results

$\lambda_{RH2O} = 4.07875 \cdot 10^{-7}$ Background $_{H2O}(1) = 1.03665 \cdot 10^{5}$

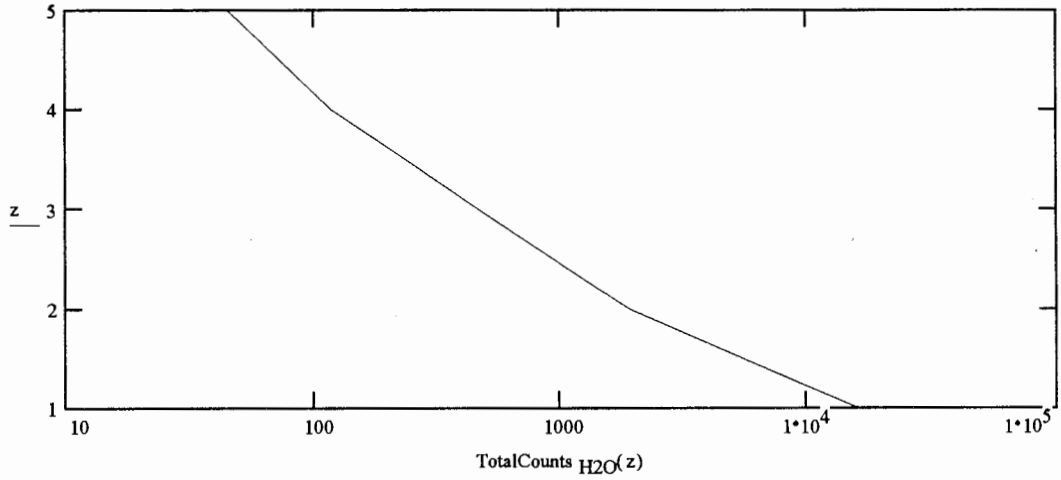

Results

$L = 266$ $B = 0$ $B_{N2} = 0$ $B_{H2O} = 1.53944 \cdot 10^{-6}$

$Background(z) := 20 \cdot 60 \cdot 30 \cdot B$

$Background(1) = 0$

$Background_{N2}(z) := 20 \cdot 60 \cdot 30 \cdot B_{N2}$

$Background_{N2}(1) = 0$

$Background_{H2O}(z) := 20 \cdot 60 \cdot 30 \cdot B_{H2O}$

$Background_{H2O}(1) = 0.05542$

$TotalCounts(z) := 20 \cdot 60 \cdot 30 \cdot N(z)$

$TotalCounts_{N2}(z) := 20 \cdot 60 \cdot 30 \cdot N_{N2}(z)$

$TotalCounts_{H2O}(z) := 20 \cdot 60 \cdot 30 \cdot N_{H2O}(z)$

z	N(z)	TotalCounts(z)	$TotalCounts_{N2}(z)$	$TotalCounts_{H2O}(z)$
1	4602.50002	$1.6569 \cdot 10^8$	$1.40124 \cdot 10^5$	4196.43207
2	128.78075	$4.63611 \cdot 10^6$	6763.1752	180.75988
3	8.10004	$2.91602 \cdot 10^5$	715.62368	16.46773
4	0.78486	28255.05099	111.88287	1.74931
5	0.10294	3705.97807	22.81129	0.30371

Molecular Scattering Results

$Background(1) = 0$

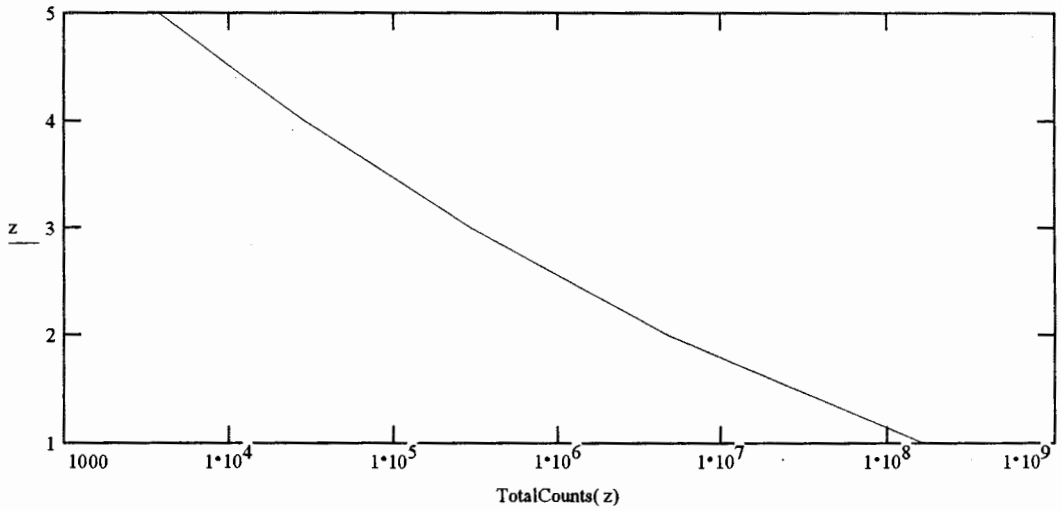

Results (cont.)

Raman Nitrogen Results

$\lambda_{RN2} = 2.83581 \cdot 10^{-7}$ Background $_{N2}(1) = 0$

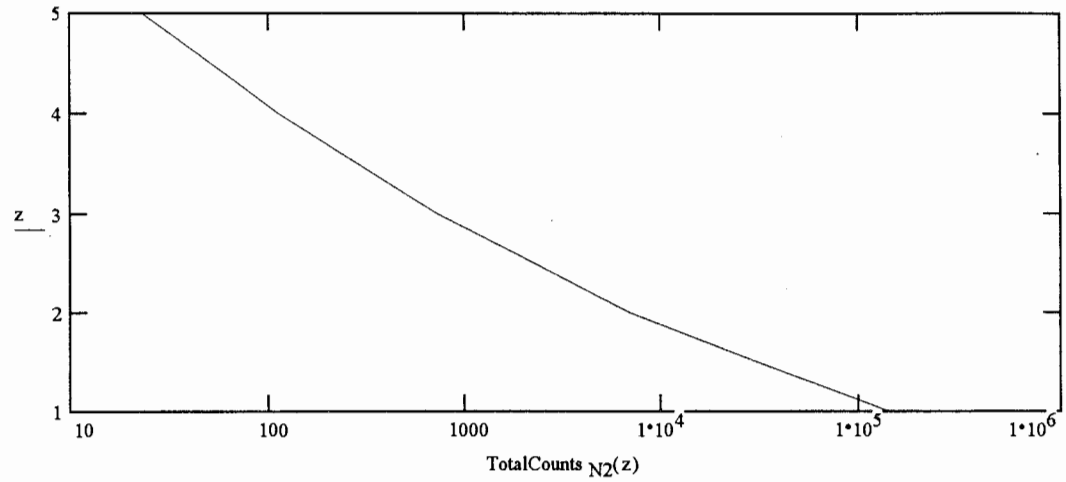

Raman Water Vapor Results

$\lambda_{RH2O} = 2.94618 \cdot 10^{-7}$ Background $_{H2O}(1) = 0.05542$

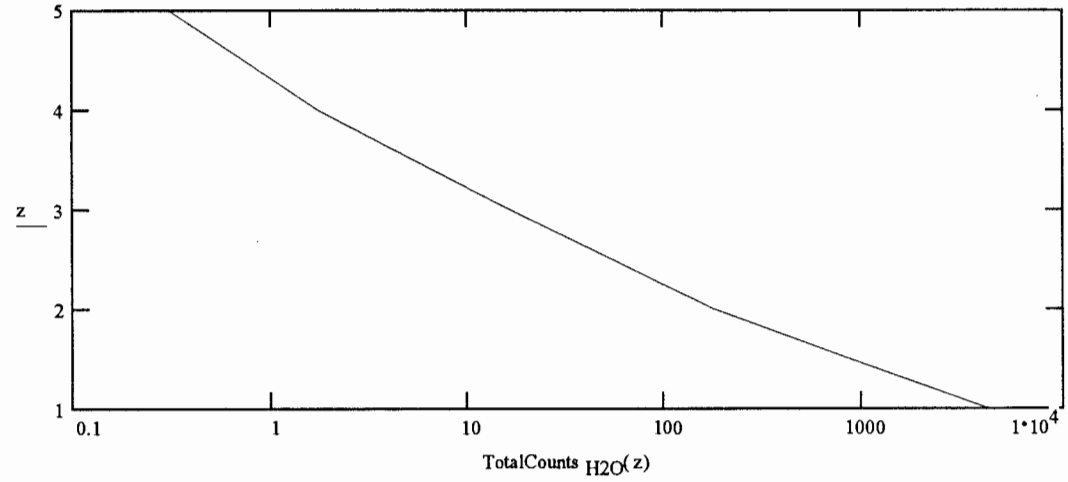

Appendix C

A Direct Doppler Detection Lidar System for Atmospheric Winds

D.W. Machuga
T.J. Kane
C.R. Philbrick

Penn State University
ARL Lidar Laboratory
University Park, PA 16802
Phone (814) 863-0851
Fax (814) 863-8457

Abstract

A new approach to sensing the wind velocity using Doppler lidar is being developed which promises to improve our measurement capability. Demonstration of this wind lidar will utilize the recently developed equipment prepared under the Laser Atmospheric Measurements Program (LAMP) at Penn State University. Development of the laser atmospheric wind sensor to profile lower and middle atmosphere winds will extend the capabilities of the LAMP instrument. This paper discusses two unique concepts which lead to advances in our ability to measure winds with Doppler lidar. One development is the quad-cavity Fabry-Perot etalon design, which will allow the etalon to simultaneously monitor the wind while under active tuning control. Several measurement campaigns will be carried out to demonstrate the wind sensor system including comparisons with met rockets, passive techniques, and radar. The second development is the use of the seed laser to stabilize the Fabry-Perot etalon continuously. Predicted system performance will be presented.

INTRODUCTION

At present, high resolution middle atmosphere wind measurements are obtained using rocket soundings, mainly by tracking a falling target (Robin sphere). Satellite remote sensing instruments can also provide low resolution wind data. Additionally, MST radars are capable of measurements in regions of aerosol scatter below 20 km, or electron scatter above 60 km during the day and 90 km at night.

Answering critical scientific questions regarding the middle atmosphere depends on more detailed observations of the dynamics of this region. For example, the heating rates caused by gravity wave breaking, and the coupling of momentum flux into the mesosphere from the wave field, and influences the vertical/horizontal transport of minor species are just a few of the important questions to be examined.

Accurate monitoring of the middle atmosphere will have more direct application to weather forecasting and lower atmospheric modeling since it couples the upper and lower atmospheric regions through influences of the global atmospheric circulation patterns. Additionally, dynamical and chemical data rely on a climatological description of the wind field. The recent developments of coupled models such as the TGCM[1], show the importance of describing the interaction between the waves and the general circulation patterns to explain global response to the increase in IR greenhouse gases. A complete understanding of the processes and a meaningful test of the theories requires simultaneous observations of the wind vector fluctuations throughout the middle atmosphere.[2] The wind sensor will be used to characterize lower and middle atmospheric dynamics. Previously unattainable data on the dynamics should allow advances in modeling efforts and weather prediction.

Lidar provides high temporal and spatial resolution which is required for dynamic studies. Several research groups have built lidar wind

sensors.[3,4,5] However, some systems are unable to maintain measurement stability of the detected wavelength or cannot accurately measure winds due to lack of aerosols above 20 km. The planned system, which is capable of high resolution wind measurement in the lower and middle atmosphere has been modeled. Two innovations which have been incorporated into the design and tuning of the Fabry-Perot etalon should allow accurate measurement of the lower and middle atmosphere winds.

INSTRUMENT DESCRIPTION

In the absence of wind, air molecules have a speed that is proportional to temperature. In any direction, the molecules have a speed distribution as shown in Figure 1a. This distribution becomes the Maxwellian velocity distribution if all speed components are integrated along one axis as shown in Figure 1b. Illuminating this volume with a laser results in a Doppler broadening of the laser pulse with the same distribution as the molecular velocities.

If there is no wind present, the curve shown in Figure 1b will remain unchanged. However, if there is wind present, the entire curve will be shifted in the direction of the radial wind. It is this shift that we wish to measure.

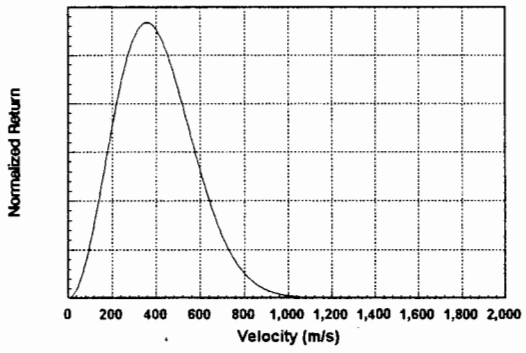

***Figure** 1**a** — Molecular Speed Distribution*

The key measurement element of the proposed wind sensor system is a quad-cavity Fabry-Perot etalon. This F-P uses several new concepts in optical coating and etalon tuning technology. The step etalon plate is shown in Figure 2. A standard quartz etalon plate has a layer of quartz deposited over one half of the surface to produce a consistent interface with a step which determines the shift of the passband from the laser center wavelength. This

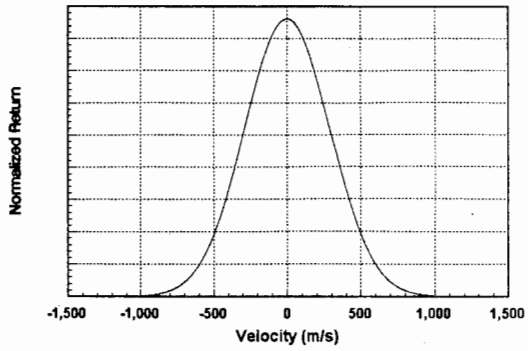

***Figure** 1**b** — Maxwellian Velocity Distribution*

plate is then finished with a standard etalon coating. If the opposite plate of the etalon is flat, this configuration permits simultaneous tuning to two different wavelengths.

If both plates are stepped with identically coated plates and rotated 90 degrees with respect to each other, then four different cavities are formed as shown in Figure 3. The two cavities of the same length, one side is stepped and the other side not stepped, are the reference cavities. If these reference cavities are tuned to the laser wavelength, the shorter and longer cavities are then tuned to the short and long half power points, respectively.

The configuration uses the seed laser for the primary laser oscillator to produce the very narrow line width (< 80 MHz) signal required. By directing a portion of the seed laser output through the

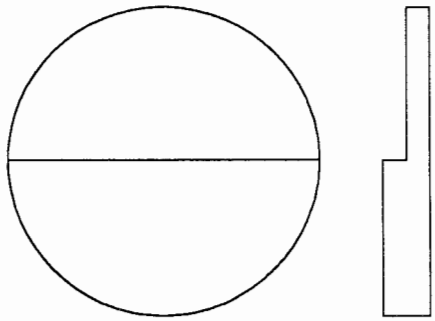

***Figure** 2 — Etalon plate showing the step increase in the thickness of the plate.*

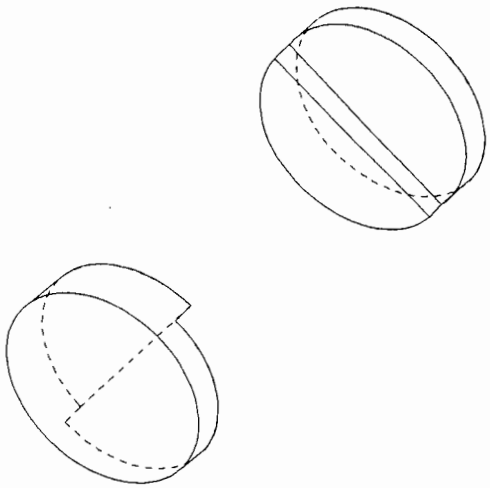

***Figure** 3 — Rotated etalon plates showing quad-cavity configuration.*

reference cavities, the etalon can be continuously optimized to the laser wavelength. Since the wavelength of the seed laser (1064 nm) is exactly double the wavelength of the laser output (532 nm), when the cavities are optimized to the seed laser, the etalon will be optimized to the half power points of the final laser output as shown in Figure 4.

Using one quad-cavity F-P, the wind velocity vector can be accurately measured. The measurement is accomplished by calculating the ratio of the two transmitted half power passband signals, which is directly related to the radial component of the wind velocity. If the wind velocity is toward the instrument, the center frequency of the Doppler broadened pulse will increase, which results in an increase in the intensity transmitted through the shorter cavity and a decrease in the intensity through the longer cavity. The opposite is true if the radial component of the wind is in the same direction as the beam. The ratio of the intensity measured at the two cavities thus provides the measure of the wind velocity.

The horizontal wind velocity component can be determined from the radial wind velocity by taking two separate measurements in orthogonal directions assuming that the vertical component is negligible. In some applications it is important to determine the vertical wind velocity, however since the vertical component of the wind is typically an order of magnitude or more smaller than the horizontal component, it can be neglected in the preliminary analysis. The initial design includes four orthogonal

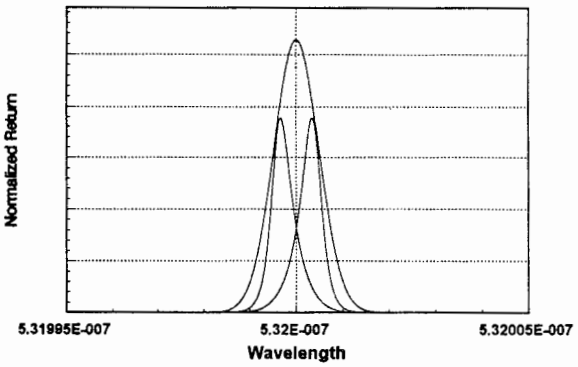

***Figure** 4 — Etalon passbands over thermally broadened laser pulse.*

measurements thereby, 1) allowing vertical wind determination using three independent direction measurements, and (2) allowing for an overly determined wind velocity vector.

PREDICTED SYSTEM PERFORMANCE

Using results obtained from the LAMP lidar with an integration time of approximately 30 minutes and a range bin of 120 meters, initial calculations yield a 1 m/s velocity resolution at 30 km. As a result, this wind sensor design should be capable of wind measurements to altitudes above 50 km with reasonable integration times. If higher altitude measurements are desired, the system is easily adaptable to a larger class of telescope and laser system.

The development of the wind sensor system including testing and intercomparisons will take place over a two year period. The first year, which will be devoted primarily to system preparation and testing, includes: manufacture of the Fabry-Perot etalon, modifications to LAMP, and initial testing with comparisons to weather balloons. The second year includes further testing and a proposed comparison with met rocket data at the NASA launch facility at Wallops Island, Va., and at Fairbanks, Alaska. The campaigns includes data matching with passive optical instruments, rocket launches, and radars.

CONCLUSION

While there are some limited data on the middle atmosphere, it still remains largely unmonitored. By using several innovative techniques,

a new method for Doppler lidar measurements of the middle atmosphere has been suggested. The system allows for wind measurement in the lower and middle atmosphere using a two new concepts. The use of the seed laser permits the required 1 MHz reference accuracy to measure wind, and the stepped etalon both will be major advantages. Other measurements also benefit from this development including more accurate temperature profiles obtained in the lower atmosphere since this system is not as susceptible to the aerosol scattering as are other molecular scatter (elastic) lidars.

ACKNOWLEDGEMENTS

The authors would like to acknowledge ARL, NSF CEDAR Program, SPAWAR PMW-165 Navy Environmental Systems Program Office, and the Penn State College of Engineering. Thanks are also due to Tim Stevens, Paul Haris, Subha Maruvada, Sumati Rajan, Prof. Roger Smith, and Dan Lysak for their contribution and support.

REFERENCES

1. Roble, R., M. Kelley and C.S. Gardner, Global change: Upper atmospheric research and the role of the NSF CEDAR program, *The Cedar Post*, 15, C.S. Gardner Ed., February 1992.

2. A Doppler LIDAR for Measuring Winds in the Middle Atmosphere, M.L. Chanin, A. Garnier, A. Hauchecorne, J. Porteneuve,Geophys. Res. Let., 16, 1273-1276, 1989.

3. Observations of Winds with an Incoherent Lidar Detector, V. J. Abreu, J. E. Barnew, P. B. Hays, App. Optics, 31, 4509-4514, 1992.

4. Description of a Doppler Rayleigh LIDAR for Measuring Winds in the Middle Atmosphere, A. Garnier, M. L. Chanin, App. Physics B55, 35-40, 1992.

5. Initial Doppler Rayleigh Lidar Results from Arecibo, C. A. Tepley, S. I. Sargoytchev, C. O. Hines, Geophys. Res. Let., 18, 167-170, 1991.